

# Characteristics of the Galileo Probe Entry Site from Earth-Based Remote Sensing Observations

Glenn S. Orton<sup>\*1</sup>, Brendan M. Fisher<sup>\*†1</sup>, Sarah 'P.' Stewart<sup>\*2</sup>, Jose Luis Ortiz<sup>\*3</sup>,  
Milena Marinova<sup>4</sup>, Sasha Hinkley<sup>†5</sup>, Viswanathan Krishnan<sup>†6</sup>, Milan Masanovic<sup>†7</sup>,  
Jelena Tesic<sup>†7</sup>, Andreas Tziolas<sup>†8</sup>

Sept emb(111,1997

Short title: *Probe Entry Site Remote Sensing*

Submitted to: *Journal of Geophysical Research - Planets*

Figures: 19

Tables: 1

Send correspondence to:

G. S. Orton, JPL 169 237, 4800 Oak Grove Dr., Pasadena, CA 91109

go@orton.jpl.nasa.gov

\* Visiting astronomers at the Infrared Telescope Facility, which is operated by the University of Hawaii under contract from the National Aeronautics and Space Administration.

<sup>†</sup> Summer Undergraduate Research Fellow, Jet Propulsion Laboratory, California Institute of Technology.

<sup>‡</sup> NASA/NRC Resident Research Associate.

<sup>1</sup> Earth and Space Science Division, JPL, California Institute of Technology, Pasadena, California 91109.

<sup>2</sup> Division of Geological and Planetary Sciences, California Institute of Technology, Pasadena, California 91125.

<sup>3</sup> Instituto de Astrofisica de Andalucia, CSIC, Apdo 3004, 18080 Granada, Spain.

<sup>4</sup> Department of Computer Sciences, California Institute of Technology, Pasadena, California 91125.

<sup>5</sup> Reed College, Portland, Oregon 97202-8199.

<sup>6</sup> Trinity College, University of Cambridge, Cambridge, CB3 9EW, United Kingdom.

<sup>7</sup> School of Electrical Engineering, University of Belgrade, Bulevar Revolucije 73, 11000 Beograd, Yugoslavia.

<sup>8</sup> University of Leicester, University Road, Leicester LE1 7RH, United Kingdom.

### Abstract

Earth-based observations indicate that the Galileo Probe entered a 5- $\mu$ m hot spot, a region of unusual clarity and dryness. This feature was in the process of evolving both to a larger size and lower atmospheric opacity when the Probe entered on 19:35 1 December 7. The Probe entered the atmosphere some 600 - 120(1 km north of the southern boundary of the hot spot, defined by a 4.78-/1111 observed brightness temperature greater than 240 Kelvins. This was S011}(" 600 km South of the center of the hot spot, where the atmospheric transmission was slightly higher, and the atmospheric declivity a few percent lower. There is a strong correlation of 5- $\mu$ m flux with 953-nm reflectivity but a weak one with 410-11111 reflectivity. The visible and near-infrared reflectivities of hot spots are remarkably similar, even for a variety of features with divergent 5- $\mu$ m emissions. Zonal structures in the tropospheric temperature field near the Probe entry site were not correlated with the location of 5- $\mu$ m hot spots but moved at speed closer to the internal rotation rate of the planet. Tropospheric wave content at the Probe entry latitude shows little correlation to the 5- $\mu$ m hot spot wave character (Ortiz *et al.* 1997). Stratospheric temperatures do not show any significant structure over 5- $\mu$ m hot spots in general or the Probe entry site specifically. Future analysis of the thermal structure in conjunction with mid-infrared data sensitive to cloud opacity will further characterize the tropospheric clouds as well as extend our temperature maps to deeper levels.

## INTRODUCTION

Long before the arrival of the Galileo spacecraft in the vicinity of Jupiter, the value of remote sensing of the Probe entry site was recognized. Despite the disparity of the spatial scales sampled by *in situ* vs. remote sensing experiments, a comparison of the two sets of data remained the most straightforward means to generalize Probe experiment results to the planet as a whole. This is particularly true because Jupiter's atmosphere is very inhomogeneous. Such a comparison would also provide a measure of ground truth against which the atmospheric properties retrieved from remote sensing instrument data might be compared.

A detailed sequence of observations by the Galileo Orbiter remote sensing instruments were planned for the time of the descent of the Probe into Jupiter's atmosphere. A system of earth-based observational support was also established in order to supplement the spacecraft data. The relatively low telecommunications rate of the Orbiter, precluding direct transmission of the data to the earth, together with limited space on the tape recorder, limited the spatial coverage of the atmosphere. Therefore, the effect of more distant phenomena, such as zonal waves whose influence extended to the Probe entry site, would be missed by the Orbiter but not by observers on the earth. Earth-based facilities could also supplement the wavelength coverage of the Orbiter instruments themselves. For example, the  $7.8\text{-}\mu\text{m}$   $\text{CH}_4$  spectral emission band, used to determine the 10-mbar stratospheric temperatures (see Orton *et al.* 1990), was not observable with the chosen Orbiter instruments, but it was observable from the earth. Earth-based observations provided the only means to track the evolution of the feature into which the Probe entered. Jupiter was heading towards solar conjunction at the time of the Probe entry, and earth-based observations were difficult as Jupiter was only  $9^\circ$  from the sun.

The anomalous behavior of the tape recorder shortly before arrival at Jupiter prompted the Cassini team to not run the tape recorder at all during the initial approach to Jupiter, including the time of Probe entry. The support of the earth-based observational program thus gained far more significance than anyone could have imagined only a few months prior to the Probe entry.

The Probe entered a relatively clear and dry area of the atmosphere known as a  $5\text{-}\mu\text{m}$  hot spot, a prominent feature representing a relatively rare set of atmospheric conditions on the planet (Orton *et al.* 1996). In addition, the Probe began to make direct observations only after descending to the  $\sim 0.4\text{-bar}$  pressure level. This was below atmospheric levels expected to contain significant cloud and haze layers (see the brief summaries of historical characterizations of the vertical cloud structure in the reports by the Nephelometer (NEP) team, Ragot *et al.* this issue, and the Net Flux Radiometer (NFR) team, Sromovsky *et al.* this issue, as well as a review of information up to that date by West *et al.* (1986)). Thus, the determination of the properties of those overlying layers would also provide information to the Probe investigations to assess their influence on analysis of the NEP and NFR data, in particular to complete the picture of the  $\text{NH}_3$ -level cloud only incompletely determined by these two instruments.

Some measurements of Jupiter were made almost simultaneous with the time of the Probe entry, despite the proximity to the sun. The proximity to the sun often compromised the quality of the angular resolution and also the available wavelength range. For example, the NASA Infrared Telescope Facility (IRTF) used a polypropylene sheet covering the entire primary permitting almost no radiation shortward of  $5\text{-}\mu\text{m}$ . This procedure also reduced substantially the signal to noise ratio of the observations. Therefore, we experimented with alternative approaches to study the PES, including a timewise linear interpolation of data taken before and after the time of the Probe entry and a study of analogous regions.

In this paper we will address these issues, refining our initial analysis (Orton *et al.* 1996) of the properties of the atmosphere as they relate to and supplement the measurements made by the Galileo Probe.

#### MORPHOLOGY OF THE PROBE ENTRY SITE REGION OVER TIME

A long time series of images of Jupiter in the 5- $\mu\text{m}$  window is described by Ortiz *et al.* (1997). These data are dominated by observations made with the 4.78- $\mu\text{m}$  narrow-band filter used with the facility near-infrared camera, NSFCAM, at the NASA Infrared Telescope Facility (IRTF) at the summit of Mauna Kea (Rayner *et al.* 1993). Figure 1 illustrates the changing morphology of the 5- $\mu\text{m}$  hot spot that evolved into the Probe entry site (PES). We will henceforth refer to this feature as the PES hot spot. The 18 panels in Fig. 1 were selected from 64 separate images which tracked this feature between 1995 March and 1997 August. This data set, described much more fully by Ortiz *et al.* (1997), is part of an even larger data set taken by IRTF staff on a regular basis in support of the Galileo mission when NSFCAM was scheduled for observations of any kind.

The first images in this data set (Fig. 1) show the presence of a hot spot at the PES, at the beginning of our data set, assuming that the spots were all moving eastward at about 103 m/sec relative to System III (Ortiz *et al.* 1997). From May to August, 1995, the PES hot spot appears to have split several times. During such episodes, our approach to tracking the feature was to match the general phase speed of all the 5- $\mu\text{m}$  hot spots with respect to System III. In 1995 September, the PES hot spot seems to have merged with another hot spot and split again shortly afterward. At the beginning of what we might call its “life cycle”, *i.e.* between 1995 Oct. 3 and Oct. 13, the hot spot re-emerged as a small wedge shape evolving into a larger comma shape, with a bright, but small round core and a small “tail”. Then, a transient filament-like morphology appeared, after which it evolved into a “mature phase” when the spot covers an area of a few degrees in longitude and had a tail tilted  $\sim 30^\circ$ . Subsequently, it reached its most intense state, flattening and expanding enormously. The PES hot spot remained in this flat morphology for some time, approximately 1995 November through 1996 July. Following this, it began its “life cycle” again, assuming a small wedge shape, followed by a comma shape. No “lustre phase” appeared during the cycle before beginning again as a small feature in 1996 December. Its 1997 evolution includes a “mature phase”, according to our most recent observations in August (Fig. 1).

Accompanying its morphological evolution were regular variations of the intensity of the hot spot over time. The PES hot spot appeared to brighten after its 1995 October life cycle began. It brightened again a few weeks after the Probe entry. The evolution of the PES hot spot intensity is shown in Fig. 2, using the full set of images from which Fig. 1 was built. For this plot, the intensity has been averaged over a region  $8^\circ$  in longitude and by  $6''$  in latitude, around the PES longitude-shifted location. Images with the PES hot spot emitting at an angle greater than  $60^\circ$  (emission angle cosine,  $\mu > 0.5$ ) were rejected. The speed used to keep the spot centered was tied to a value which varied slowly with time. We used 103.5 m/s for the period 1995 March - December, 102.5 m/s from 1996 January - May, 101.5 m/s from 1996 June - December and 100.5 m/s from 1997 January - July, as these provided a best match with the phase speeds of all observed 5- $\mu\text{m}$  hot spots around the circumference of the planet.

The upper graph in Fig. 2 was made using the complete set of calibrated images, whereas the bottom graph has been made with a more restrictive  $\mu$  cutoff (0.4) and also using an alternative means of absolute calibration, scaling the total counts in a region  $60^\circ$  by 1600 around the center of the disk. This assumes that the brightness of nearly the whole disk does not change significantly in time, which is not strictly true. For the lower graph, we have included the radiance at the date

of probe entry although the spatial resolution of this image was worse than the rest of the images. For that image alone, we manually calculated the total flux within a larger area. The error bar of the radiance at the time of entry has been calculated by using several synthetic apertures of different sizes. For the rest of the points, the errors have been assigned as 20% of their brightness. The overall shapes of both curves agree reasonably well, although the maxima are higher for the first calibration method.

Figure 2 shows that the PES brightness reached its maximum within 2 months after probe entry, a brightness equivalent to a temperature around 255 K, although the core of the PES hot spot must have reached higher temperatures, as we are plotting averages within an area  $8^\circ$  by  $6^\circ$  wide. The peak temperatures we can detect from the ground are very sensitive to seeing variations, which limits our spatial resolution. With these caveats in mind, the highest  $4.78\text{-}\mu\text{m}$  brightness temperature we have ever observed at the PES hot spot was 265 K ( $0.54\text{ W/m}^2/\mu\text{m/sr}$ ), coincident with the time of maximum spatially averaged intensity. We note that these images were often accompanied by observations of stellar standard stars which, in the future, will allow us to verify these apparently large variations with time for observations unvignetted by the telescope dome, at least 30 days from solar conjunction.

### THE PROBE ENTRY SITE AT TIME OF ENTRY

Because much analysis of the Probe data depends on our determination that the Probe entered a  $5\text{-}\mu\text{m}$  hot spot, we thought it wise to verify this conclusion and make improvements to our original estimates of its location within the hot spot. While it was crucial to determining the morphology and radiometry of  $5\text{-}\mu\text{m}$  hot spots (see above and Ortiz *et al.* 1997), the NSFCAM instrument was susceptible to saturation during the time of the Galileo Probe entry because of the immense background noise added by the polypropylene safety screen in the optical path. We had better success imaging Jupiter with a broader  $4.80\text{-}\mu\text{m}$  (M-band) filter on the MIRAC2 instrument (Hoffmann *et al.* 1993) in early December, 1995, at the time of the Probe entry, and with the Jet Propulsion Laboratory's MIRLIN instrument (Ressler *et al.* 1994) in early January, 1996. Both of these instruments were much less sensitive in the  $5\text{-}\mu\text{m}$  region and had deeper electronic wells than NSFCAM. As a result, they were much less sensitive to saturation).

As explained by Orton *et al.* (1996), making accurate estimates of the position of the Probe entry site (PES) within the  $5\text{-}\mu\text{m}$  hot spot is complicated by the low angular resolution of the MIRAC2 M-band images taken during the epoch of the Probe entry. This is simply an inherent problem associated with observing so close to the sun, complicated by the high attenuation of the safety screen which required cumulative integration times of tens of seconds. For comparison, NSFCAM cumulative integration time is  $\sim 2$ -second, using only images with the highest quality seeing. Our alternative estimate of the entry position assumed that the  $5\text{-}\mu\text{m}$  feature was stable in size and location between late November of 1995 and late January of 1996. The PES hot spot appeared to be stable and roughly constant in size and shape between the two  $5\text{-}\mu\text{m}$  observations made at the NASA IRTF without the safety screen in late November of 1995 and late January of 1996, even though its brightness increased substantially (Fig. 1). Comparing the nominal entry latitude and longitude of the PES with the morphology and position of the  $5\text{-}\mu\text{m}$  spot interpolated between these two dates appeared to be a reasonable first-order approach to overcoming the deleterious effects of the reduced seeing while the safety screen was used with the telescope. Figure 3 shows that such an interpolation in time is fully consistent with the actual observations of the  $5\text{-}\mu\text{m}$  hot spot associated with the PES during this time. The PES  $5\text{-}\mu\text{m}$  hot spot did not undergo splitting or migration with respect to a largely constant local eastward flow with respect to System

Figure 4 indicates the nominal PES location on the 5- $\mu\text{m}$  hot spot. We note that these images (and those in Fig. 3) have been further processed than the equivalent images displayed in Fig. 2 of Orton *et al.* (1996). First, rather than using the best image made on each date, several high-quality images were selected for averaging from a 2-minute time interval to minimize blurring by planetary rotation. Some additional care was taken to optimize the assumptions about the seeing function used in image restoration (see Ortiz *et al.* 1997, for details of this process). If we adopt the criterion of Ortiz *et al.* (1997) that hot spot regions are defined by thermal radiances with an equivalent brightness temperature greater than 240 Kelvins, then both the 1995 November and 1996 January images and, logically, the interpolated image immediately confirm that the PES was, indeed, located inside the 5- $\mu\text{m}$  hot spot. Using this criterion, and keeping in mind that, the size of a pixel in these cylindrical maps is just over 600 km, the PES appeared to be close to the southern boundary of the 5- $\mu\text{m}$  hot spot, with the southern edge located between 600 and 1200 km (i.e. 1 and 2 pixels) away. For the November image, the boundary was within 600 km (1 pixel) south, and for the January image it was 1800-2100 km (2 - 3 pixels) south. We can say that the PES was something like 3000 km (and certainly more than 1200 km) south of the northern boundary of the feature, although the assumption that we can predict the morphology of the highly evolving, northern boundary of the hot spot by timewise linear interpolation is somewhat suspect. The uncertainty of this position is dominated by the geometric calibration of these images, an angular size which is equivalent to 670 km when projected on the disk at the PES - not far from the value of the spatial resolution. This value represents 1 standard deviation, and it is an improvement over the estimates of Orton *et al.* (1996): the cover of the 1996 May 10 issue of *Science* shows a 2 standard deviation circle around the PES. This estimate was made on the basis of (1) reproducibility of the PES geometry for several other days with similar quality seeing in November, and (2) estimates of the intrinsic uncertainty of fitting the sharp 5- $\mu\text{m}$  limb of the planet under conditions of 0.3 - 0.5 arcsec seeing, characteristic of the actual observing conditions.

The 4.78- $\mu\text{m}$  brightness temperature of the PES is measured as 248.6 K, with less than 0.3 K variations within 1200 km east of west. This value is interpolated between 242.8 K in 1995 November and 260.3 K in 1996 January. It is consistently  $0.5^\circ$  (1 pixel) south of the brightest area of the feature which is approximately 1 Kelvin higher in brightness temperature.

#### THE PROBE ENTRY SITE IN THE VISIBLE

Figure 1 of Orton *et al.* (1996) shows the PES with respect to observations of reflected sunlight in red and near-infrared wavelengths taken from observations at Pic-du-Midi Observatory and the Swedish Solar Telescope. While consistent with the PES being located inside a region of lower reflectivity than the surroundings, these images, taken within a few days of the Probe entry time, suffer similar seeing degradation as for the 5- $\mu\text{m}$  images. Unlike the 5- $\mu\text{m}$  images, however, there is no high contrast associated with the hot spot which allows a robust image restoration algorithm to be applied (see the description in Ortiz *et al.* 1997). Thus, while 1.58- $\mu\text{m}$  images were also taken on November 21, 1995, and January 23, 1996, they do not provide a better description of the darker albedo associated with the entry site. Therefore, we decided to examine comparisons between the PES hot spot at 4.85  $\mu\text{m}$  and the highest possible spatial resolution observations in the "visible" range from the Wide-Field / Planetary Camera (WF/PC2) on the Hubble Space Telescope.

We examined the PES hot spot using WF/PC2 at wavelengths shortward of 1  $\mu\text{m}$  during periods both before and after the probe entry: 1995 March 5, 1995 October 4 and 5, 1996 May 14, and 1996 June 27. The 1995 October and 1996 June data were taken within 24 hours of 1 RTFNSFCAM

observations (Table 1). The PES hot spot has evolved little in this short time span, allowing direct comparisons of the morphology in the two wavelength regimes to be made. The HST images were calibrated using the procedures discussed by West *et al.* (1994), and we adopt a  $\sim 5\%$  error level, which is supported by Chanover *et al.* (1996). In order to facilitate intercomparison of the filtered photometry of the various hot spot regions, we solved for the coefficients of a Minnaert function which was applied to the observed data. The data were then adjusted from observational values of the emission and incident sunlight angle cosines,  $\mu$  and  $\mu_0$ , respectively, that ranged from 0.55 to 0.95, to a common value of 0.70. For the 953-nm data, the sum of the values of the powers used for  $\mu$  and  $\mu_0$  in the Minnaert function were significantly less successful if their sum was fixed to unity than for a higher value, so we adopted the latter. We adopted these adjusted values for all discussions of the HST data on the PES.

Figures 5 and 6 plot the correlation between the 4.78- $\mu\text{m}$  radiance and the reflectivity from the 953-nm and 410-nm filters, representing the endpoints of the “visible” spectra for the 1995 October and 1996 June data, respectively. Clearly there is a class of cold points at 4.78  $\mu\text{m}$ , with radiance less than  $0.07 \text{ W/m}^2/\text{ster}/\mu\text{m}$  (224 K brightness temperature), particularly prominent in the 1995 October data set, representing a wide range of relatively high reflectivities at both 953 nm and 410 nm. These points correspond to regions in the lower half of the images, which are portions of the Equatorial Region. Regions with higher 4.78- $\mu\text{m}$  radiances are clearly correlated with lower 953-11111 reflectivity, so that our 240-Kelvin brightness temperature criterion ( $0.18 \text{ W/m}^2/\text{ster}/\mu\text{m}$ ) corresponds to  $I/F < 0.60$ . For a given 4.78- $\mu\text{m}$  radiance, the spread of  $I/F$  values at 953 nm is 0.05 or less for 1995 October and  $\sim 0.08$  for 1996 June when the ground-based seeing was poorer.

On the other hand, the correlation between 4.78- $\mu\text{m}$  radiances and 410-nm reflectivity cannot be nearly so well established. The absolute correlation coefficients are 0.501 less, and the spread of  $I/F$  values for a given 4.78- $\mu\text{m}$  radiance is  $\sim 0.20$  at best.

Figure 7 and 8, plotting the reflectivity as a function of latitude at these two wavelengths, offer some clarification. For both epochs of observation, the PES is a distinct feature at 953 nm, but much less so at 410 nm. As a distinct feature, the PES has much lower contrast at 410 nm, and its northern boundary merges with the lower reflectivity of the North Equatorial Belt at higher latitudes.

We note that the reflectivity of the PES latitude,  $6.5^\circ \text{N}$ , is brighter than the darkest part of the PES, a degree or two north, by only 0.03 or less at 95311111. The 410-nm reflectivity of the PES is 0.04-0.05 larger over the same distance. Figures 9 and 10 show the spectrum of the PES and the darkest areas of the PES feature (as measured at 953 nm), respectively, as a function of time. We note that the reflectivities do not vary much over time, compared with the errors of measurement (with the possible exception of the 555-nm point in 1995 March). A comparison of the two figures also shows that the small differences in  $I/F$  between  $6.5^\circ \text{N}$  and the “center” of the feature apparent in Figs. 7 and 8, are generally true for the other observations, as well. Figure 11 shows a similar spectrum for a 5- $\mu\text{m}$  hot spot some  $40^\circ$  away in longitude. Its similarity to Figs. 9 and 10 is also persuasive that the “visual” reflection spectrum of all hot spots is very similar.

#### CLOUD PROPERTIES AT 5- $\mu\text{m}$ HOT SPOTS AND THE PROBE ENTRY SITE

A major examination of cloud properties at the PES and comparison with other 5- $\mu\text{m}$  hot spots is given by Stewart *et al.* (1997), based on a detailed analysis of near-infrared data from the NASA IRTF. By using a single-scattering cloud inversion technique, they are able to retrieve the vertical cloud structure without any *a priori* assumptions about the cloud levels. They detect three cloud levels throughout the northern Equatorial Zone (EZ) and southern North Equatorial Belt (NEBs):

a thin stratospheric haze layer distributed  $\geq 20$  mbar, an upper tropospheric cloud based between 350 and 460 mbar, and a lower tropospheric cloud with an effective cloud top between 1.5 and 3.0 bar. The upper two cloud layers are optically thin at  $2.0 \mu\text{m}$ , with optical depths of  $\leq 0.01$  and  $\sim 0.5$  respectively.

Stewart *et al.* (1997) find that the upper tropospheric cloud is very homogeneous throughout the north equatorial region, including several hot spots and plumes. There are only slight differences in cloud elevation and opacities between hot spots and their surrounding regions, implying that at altitudes greater than the 1-bar level, hot spots are not significantly different than the rest of the EZ and NEBs. These results are consistent with a study using HST data at 893 and 953 nm by Chanover *et al.* (1997). They found only a 20% difference in opacity between hot spots and plumes at the probe entry latitude in the upper tropospheric cloud layer.

Further evidence of the relative homogeneity of this cloud layer is the visible spectra of  $5\text{-}\mu\text{m}$  hot spots. Although the morphology and  $5\text{-}\mu\text{m}$  radiance of the PES hot spot changed considerably in 1995 and 1996 as described in previous sections, the visible spectrum did not. In this wavelength range, there is little variability in the spectra over time and also between the PES hot spot and its companion hot spot. This analysis supports our approach of using analogous regions in the study of the upper tropospheric cloud in the PES hot spot.

There is a difference, however, in the absolute opacity of the upper tropospheric cloud between visible and NIR observations. An optical depth of 6.0 at  $\sim 900$  nm is required for hot spots in the model presented by Chanover *et al.* (1997). The sharp decrease in opacity between the visible and NIR imply that the cloud particles in this layer are very small,  $r < 1 \mu\text{m}$ . Such small particles have only a small influence in the atmospheric opacity at  $5 \mu\text{m}$  and the slight decrease in opacity over hot spots cannot be the sole mechanism responsible for the strong  $5\text{-}\mu\text{m}$  radiation through hot spots.

Previous work, summarized in West *et al.* (1986), suggest that the lower tropospheric cloud is more heterogeneous than the upper tropospheric cloud and may play a larger role in the dynamics of hot spots. Stewart *et al.* (1997) corroborate this hypothesis, but the interaction between these two cloud layers in the formation of a  $5\text{-}\mu\text{m}$  hot spot is not yet understood. The upper tropospheric layer will not play a significant role unless it contains a large particle component as suggested by Voyager IRIS observations (Carlson *et al.* 1993). Further constraints on the role of each cloud level may be made by observations at longer wavelengths which will be extremely useful in providing constraints on the extent of the distribution of large particles in the clouds.

Based on the cloud model presented in Stewart *et al.* (1997), the upper tropospheric cloud may have been out of reach by the Galileo nephelometer experiment which did not begin measurements until the 0.4-bar level. Unfortunately, the optical properties of the particles in this layer remain poorly characterized. Extension of cloud models developed in the NIR towards shorter wavelengths cannot be done in a straightforward manner because the optical properties of the cloud particles is complicated by the presence of chromophores. Once a robust vertical cloud model is compiled, close examination of the properties of this cloud layer in the visible may proceed with fewer free parameters.

#### TEMPERATURE FIELD AT $5\text{-}\mu\text{m}$ HOT SPOTS AND THE PROBE ENTRY SITE

We derived tropospheric temperature maps from thermal infrared data to look for connections between the temperature field in the upper troposphere and the hot spots analogous to the PES hot spot. The tropospheric temperature fields were derived from thermal infrared data acquired at the NASA IRTF. Data reported here were gathered in three epochs. The first epoch was in



1995 November, prior to the Probe entry, the second in 1995 December overlapping with the time of Probe entry, and the third in 1996 January, approximately one month after the Probe entry. The data for November and December of 1995 were acquired with the MIRAC2 imaging infrared camera while the 1996 January data were acquired with the MIRLIN imaging infrared camera. To retrieve temperatures, we used MIRAC2 data taken at wavelengths of 13.3, 17.4, 17.8, and 20.6- $\mu\text{m}$  and MIRLIN data taken at wavelengths of 17.9, 18.7, and 20.8- $\mu\text{m}$ .

The data consist of full-disk images through discrete, broad-band ( $\sim 0.5$ – $1.5 \mu\text{m}$  widths) filters. Standard mid-infrared data reduction techniques were followed to produce the individual images. The radiance from Jupiter was separated from the emission of the terrestrial sky by subtraction of short-term sky variations at high frequency using the telescope secondary to provide successive images of the object and the sky (“chopping”). Longer-term drifts of the sky or telescope emissivity were removed by additional subtraction of a similar “chopped” pair with the telescope pointed at the nearby sky (“nodding”). Such images from the IRTF with MIRAC2 have been published from the epoch of the Shoemaker-Levy 9 impact with Jupiter (Orton *et al.* 1995). Observing conditions, combined with the need to use a solar shield in December resulted in a signal-to-noise ratio of about 80–100 per pixel for the individual images. Conditions were better in November, resulting in a SNR of about 150 for individual images. Images in January have a SNR of about 40.

The data were absolutely calibrated using observations of  $\alpha$  Boo taken during each epoch with the same observing method. However, star data were not available on each day in a given epoch. When same-day star data were not available within an epoch, Jovian images taken on a day with stars were first calibrated to form a reference set. Jupiter data from other days in the same epoch were calibrated against the reference set by doing a least squares fit between central meridian scans of each image, averaged over  $10^\circ$  of longitude. The uncalibrated image was then scaled to the reference image, based on the central meridian fit. For days where stellar reference measurements were made, absolute calibration is within 10% of the radiance expected from estimates based on Voyager IRIS north/south scan data for these same wavelengths. The relative calibration technique limits our sensitivity to temperature perturbations and wave-like structure on spatial scales on the order of one-third of the planetary circumference (wavenumber 3 or lower), which is much larger than PFS hot spot spatial scales.

After calibration the data were cylindrically projected onto an even,  $10 \times 1^\circ$ , grid. For these projections, we used Jupiter’s System-III rotation rate for longitudinal placement. The rotation rate of the thermal structures have been observed to be very close to the System-III rate,  $\sim 10 \text{ m sec}^{-1}$  (see Deming *et al.* 1989, 1997, Orton *et al.* 1994, Magalhães *et al.*, 1989, 1990). The rotation rate of the thermal features is also independent of latitude. We have therefore added all available maps in a given epoch together, strictly in System III, to form a composite map with the best possible longitudinal coverage. The small rotation rates of the features with respect to System III only results in drifts of approximately 260 km over three days, the typical span of our observation epochs, well below our diffraction-limited spatial scale of  $\sim 12400 \text{ km}$ . The slow rotation rate was also confirmed by examining regions of overlapping longitudes from maps on different days. In the overlapping regions, the longitudinal structure was aligned in System III, as expected. We show the composite map for the 250-mbar pressure level for December, 1995 in Figure 12.

The choice of wavelengths was made to sample the spectrum where it is dominated by the collision-induced opacity of  $\text{H}_2$ , and it was modeled by an appropriate combination of  $\text{H}_2$ - $\text{H}_2$  and  $\text{H}_2$ -He collision-induced absorption (Birnbaum *et al.* 1996). Our filter selection provides sensitivity to temperatures in a pressure range between about 250 and 400 mbars. We choose the non-

linear weighted-Chahine technique (Chahine 1970) for its ease of implementation and robustness with a data set where observations at all filters is occasionally not available at each point on the planet. As significant time separated successive images at different wavelengths, the data were combined by first projecting them onto a cylindrical coordinate system with equal latitude and longitude grid points. The observational data for each grid point (latitude, longitude pair), consisting of wavelength, brightness temperature, and emission angle, was assembled from the various cylindrically projected images. The atmosphere was not sounded deeper than 316-mbar pressure, as the influence of a cloud of  $\text{NH}_3$  particles (e.g. Orton *et al.* 1982; Gierasch *et al.* 1986) could have an important effect at this depth, and we were not yet prepared to separate the temperature and cloud opacity fields from each other at the time of this writing. Data were taken only from positions on the planet where the emission angle was greater than  $\mu \sim 0.40$ , as our diffraction-limited angular resolution would combine the influence of cold space any closer to the planetary limb.

The set of temperatures retrieved from each of the three observing epochs was combined into a single temperature map which characterizes the epoch as a whole. The PES (6.5° N latitude, 5° W longitude, System III) on 1995 December 7 is, in fact, covered by these maps. Using these composite maps, we can examine the tropospheric temperature field over the PES hot spot, as well, and examine other hot spots at the same latitude. While the longitude of the PES hot spot is covered by the maps, there can be no direct correlation between a given temperature structure and a 5- $\mu\text{m}$  hot spot because of very different rotation rates. Within a single day, the 5- $\mu\text{m}$  hot spots will drift approximately 7° with respect to System III (Ortiz *et al.* 1997), while the temperature structure remains essentially unmoved. The fact that there is no measurable difference between the tropospheric temperature inside and outside of hot spots was also noted by Orton *et al.* (1997) for Galileo Photopolarimeter Radiometer (PPR) experiment measurements of the 250-mbar temperature of a region which included a 5- $\mu\text{m}$  hot spot.

The temperature structure in the stratosphere was characterized by a single set of observations sampling the strong  $\nu_4$  fundamental band of  $\text{CH}_4$ , a vertically well mixed gas. These were made with a circular-variable filter at a position of 7.85  $\mu\text{m}$ , with a 2.5% full-width at half maximum. These observations, vertically well separated from the upper troposphere, allowed us to derive temperatures at the 10-mbar level, using a temperature perturbation technique similar to the one used by Orton *et al.* (1991) to determine stratospheric temperatures from raster scans of Jupiter made with a discrete filter centered at 7.8  $\mu\text{m}$ . For the 1995 December and 1996 January epochs, observations at 7.85  $\mu\text{m}$  were so severely attenuated by the polypropylene cover that we chose only to analyze the data as longitude scans at the PES latitude. We examine in greater detail the 1995 November images at 7.85  $\mu\text{m}$ , also made with MIRAC2. These are shown in Figure 17.

We have examined the longitudinal structure of the tropospheric temperature field at the PES latitude. The PES latitude is at the southern edge of the well defined warm axisymmetric band known as the North Equatorial Belt (NEB). We extracted a longitudinal strip covering 5-7° N latitude. At the time of the observations, Jupiter subtended approximately 31.5 arc-seconds. Telescope aperture and our wavelength led to a diffraction-limited angular resolution corresponding to  $\sim 10^\circ$  of Jovian latitude or longitude at the sub-Earth point. Because of the large diffraction limit, our longitude scans at 6° N are not completely independent of the main NEB longitude structure. The equator was relatively free of longitudinal structure at the time of the observations. Thus our PES-latitude scan is a combination of the true, latitudinally unresolved structure at 5-7° N latitude, as well as the prominent NEB structure and subdued equatorial structure. To reduce the

effects of systematic errors induced by independent temperature sounding for each disk, the composite longitudinal scans were produced as temperature residual scans separately for each disk map and then placed into their proper longitudinal locations. Overlap regions were averaged together after removal of the background temperature level. The composite longitudinal scans for the three epochs are shown for the 250-mbar level and the 316-mbar level in Figs. 13 and 14, respectively.

Overlapping coverage between days in an individual data set confirms that the longitudinal structure rotates close to the System-III rate. The temporal evolution and significant, longitudinal gaps prevent a meaningful derivation of the rotation rates on time scales between the epochs, which potentially could measure values as small as those previously reported (Deming *et al.* 1989, 1997, Orton *et al.* 1994, Magalhaes *et al.*, 1989, 1990). Our large diffraction limit does not allow us to constrain the rotation rates from data within an single epoch meaningfully. Some structures at the 316-mbar level seem to be stable between the 1995 December and 1996 January scans, while others clearly change or drift.

The limited data sets did not allow for complete longitudinal coverage in any of the epochs. The large gaps lead us to choose to the Lomb-normalized periodogram (Press *et al.*, 1992) for the wave content search. The Lomb periodogram technique was developed for finding the power spectra of unevenly spaced data. Its advantage in our application is that it weights the data on a pm-point basis instead of the per-interval basis of the Fourier technique. This greatly reduces the undesirable effects of the windowing function, compared to normal Fourier techniques. The Lomb periodogram technique finds the normalized power as a function of wavenumber essentially by fitting a series of sines and cosines to the data. The results of this analysis for the 250-mbar level and the 316-mbar level are shown in Figures 15 and 16, respectively. The normalization in the technique produces power levels corresponding to the probability that a given feature could be produced by random, normally distributed noise. The confidence levels are shown on the plots as a false alarm probability power level in figures 14 and 15.

Our stratospheric map, Fig. 17, shows meridional structure similar to the troposphere. Both stratosphere and troposphere are warmer over mid-latitudes. However, the stratospheric temperature maxima are located further from the equator, and at the PES latitude, the stratosphere shows very little structure down to our noise limit. Again, our analysis is limited by telescope diffraction, and longitudinal scans at the PES latitude are a convolution of the real structure and that at surrounding latitudes. We have produced longitude scans from our tropospheric data similar to those from our stratospheric data. We have produced longitudinal scans from data from September 5, November 7, and December 7, 1995, which are shown in Fig. 18. Error bars for each scan, based on the signal-to-noise ratio of the intensity data, are shown in temperature units for each scan near the right hand edge of the plot.

For comparisons with longer-term data sets, we produced zonally averaged meridional scans from the November, 1995, stratospheric temperatures, which have the best signal-to-noise ratio. The November, 1995 meridional scan is plotted in Fig. 19 with a similar scan made from August, 1994 stratospheric data (Orton *et al.* 1995). The difference between the two is marked by (a) a prominent change showing up as a warming of the equatorial region, on which is superimposed (b) a seasonally forced hemispherical asymmetry. There is strong evidence for the latter over a 10-year history covering most of a Jovian year (Orton *et al.* 1991). Leovy *et al.* (1991) suggested that Jupiter's equatorial stratosphere may undergo a "quasiquadrennial oscillation" (QO) which would be responsible for a similar quasi-periodic variation also observable in the 10-year study of stratospheric temperatures. The relative amplitudes of the equatorial and mid-latitude temper-

atures November, 1995, compared with 15 months previous to that time are consistent both in morphology and phasing with their hypothesis.

## DISCUSSION

Our intention in these studies is to compare earth-based remote-sensing characterizations of the PES with Galileo observations. This is made difficult, however, because of the evolution of the Probe entry site  $5\text{-}\mu\text{m}$  hot spot in brightness between the two points (1995 November and 1996 January) where we have some reasonable confidence in the absolute radiance calibration. It is possible that the evolution of the hot spot was not simply linear in time. The uppermost measurements in the  $5\text{-}\mu\text{m}$  channel (channel C) of the Net Flux Radiometer (NFR) are equivalent to a 255 K brightness temperature, but they are below the 450-mbar level cloud (Sromovsky *et al.* 1997). A best guess for the brightness temperature at the top of atmosphere is 23 K (A. D. Collard, pers. comm.), but this value depends on the properties of the  $\text{NH}_3$  cloud above this uppermost observation point which are derived from the analysis of the attenuation of solar radiation in the NFR short-wavelength channels. Furthermore, the brightness temperature for the broad NFR Channel C filter (Fig. 3 of Sromovsky *et al.* 1997) must also be converted to the narrower  $4.78\text{-}\mu\text{m}$  filter (Fig. 1 of Ortiz *et al.* 1997), using a spectral model. On face value, however, the relatively low brightness temperature might be interpreted as implying that the  $5\text{-}\mu\text{m}$  brightening of the PES between November and January did not occur uniformly in time but more slowly through December. We will also investigate the quality of our highly attenuated broad-band  $4.8\text{-}\mu\text{m}$  observation of Jupiter and  $\alpha$  Boo by MIRAC2 for the observing run in early December, 1995, to determine whether it could be used to verify this implication.

In comparing our results with Galileo orbiter observations, our closest analog to the PES is the G1 orbit "HOTMAP" observation by the Near Infrared Mapping Spectrometer (NIMS). This hot spot revealed higher  $5\text{-}\mu\text{m}$  intensities than any other region observed by NIMS through the G7 orbit in April, 1997 (Roos-Serote *et al.* 1997). This feature is, in fact, the PES hot spot in a later portion of its "mature" phase, identical to the feature shown as "1996 June" in Figs. 6, 8 and 10. Although our  $4.78\text{-}\mu\text{m}$  measurements of this hot spot were lower resolution than either the 1995 November or 1996 January images used to interpolate to the Probe entry time (Fig. 4), our peak brightness temperatures (242 K) are consistent with its May - June brightness history (Fig. 2) as a slowly dimming feature. This brightness temperature is lower than the 248 K PES  $4.78\text{-}\mu\text{m}$  brightness temperature we estimated for the time of entry, and we must conclude that the "HOTMAP" feature is more opaque than the PES at this wavelength. Further complicating the issue is that fact that NIMS did not recover the part of this observation in the hot spot at  $6.5^\circ$  N latitude. We can, however, examine the atmospheric characteristics recovered by Roos-Serote *et al.* (1997) from NIMS observations at an equivalent distance (600 - 1200 km) from the northern boundary of the "HOTMAP" feature, a location which, similar to the PES (Fig. 4), is within 600 - 1200 km of the location of the peak  $5\text{-}\mu\text{m}$  radiance. These are much closer to the properties they derived for the center of the hot spot than derived for their "border" sample. Even more confidence in this statement can be generated by noting that for both the PES and the "HOTMAP", observable conditions are relatively uniform within  $\sim 1000$  km of the center. By this analogy, and considering that the PES hot spot could have been even brighter at  $5\text{-}\mu\text{m}$ , we would conclude that in the model of Roos-Serote *et al.* (1997), the middle cloud transmittance could be 0.62 or more, water vapor would be 0.09% of saturation or less, and approximately the same vertical mixing ratio of ammonia gas as modeled by Sromovsky *et al.* (1996). This analogy deserves much further scrutiny in the future. We will be searching the NIMS data set for subsequent orbits for better matches between

our deduced  $5\text{-}\mu\text{m}$  properties of the PES and those of various hot spots examined by NIMS. We will also extend the analysis of the observations to shorter wavelengths.

A comparison between HST and NIMS observations of reflected sunlight also confirms a slow change of I/F over the same spatial scales. In fact, the various comparison of the visual observations in Figs. 5 - 10 shows several things relevant to characterizing observable conditions at the PES. The time variations of the short-wavelength ("submicron") reflectivity of the PES hot spot are far smaller than the variations of the  $4.78\text{-}\mu\text{m}$  radiance apparent in Fig. 2. The reflectivity of the atmosphere at precisely  $6.5^\circ$  N is slightly, but consistently higher than the center of the hot spot feature (some 600 - 1200 km distant), so that small perturbations to models using observations of hot spot centers to characterize conditions at the Probe entry site might be necessary. The relative invariance of the reflectivity across this part of the spectrum with time provides some assurance that the spectrum shown in Fig. 7 is likely to characterize the PES at the time of entry to within the 5% uncertainties of the absolute calibration, combined with the additional uncertainties shown in the figure. It is more likely that the properties of clouds toward the longer wavelengths are participating in the definition of hot spots as unique features on the planet, than are properties of the clouds at shorter wavelengths.

The reason that hot spots are better defined in the "red" than the "blue" could be related to the hypothesis that only differences in a larger particle population are involved (e.g. West *et al.* 1986). On the other hand, the effects of a large particle population appear to be negligible on these short wavelengths (Irwin *et al.* 1997). The other possibility is that different compositions of particles with different single-scattering albedo in the visible spectra are involved. These particles could be a chromophore component as suggested by the blue color of hot spots in the visible (e.g. Fig. 6).

We have not engaged in further elucidation of cloud properties from visible reflectivities or  $5\text{-}\mu\text{m}$  thermal radiances at this time, as there are a number of missing pieces of information. One of the problems with using observations from the  $5\text{-}\mu\text{m}$  spectral region alone to elucidate the cloud stratigraphy is the degeneracy of cloud models. This radiation can be influenced by atmospheric particulates down through the 6-bar level (e.g. Irwin *et al.* 1997, Roos-Scote *et al.* 1997). We have made observations of thermal radiation at  $8.57\text{ }\mu\text{m}$ , which is between strong bands of gaseous absorption by methane and ammonia and sensitive to cloud particles down to the 1-bar level. Including the analysis of data sets at  $8.57\text{ }\mu\text{m}$  taken in 1995 November and 1996 June will determine the optical thickness of the upper-level clouds in the context of the retrieved temperature structures presented here. This will allow a separation between cloud influences above and below the 1-bar level.

In the visible region, an extension of the models presented by Stewart *et al.* (1997) can be made using the HST data shown earlier. A separation between the effects of cloud optical depth and albedo must be made, however, in order to resolve which of the possibilities is responsible for the widely acknowledged unique color of the hot spots (e.g. Rogers 1995). In order to do this, HST (and other) imaging observations of hot spots at different emission angles are required, extending the type of work to other wavelengths begun by Chanover *et al.* (1997). A robust cloud model must be developed over a large range of wavelengths to overcome the question of uniqueness.

Closely related to the issue of cloud formation is the distribution of ammonia gas. If the upper tropospheric cloud presented in Stewart *et al.* (1997) is the main ammonia cloud at the condensation level, the ammonia mixing ratio is only a few percent of solar throughout the equatorial region. Collard *et al.* (1997) determined that the equatorial region is depleted in water relative to solar

abundances by fitting spectra taken with the CSHELL spectrograph at the IRTF. These results imply that the entire equatorial region may be depleted in volatiles. Thus the abundances in hot spots may not be as unique as originally thought. A very dry downdraft would not be a necessary explanation for hot spot abundances relative to their immediate surroundings. These analyses will also be performed at regions of expected upwelling at  $\pm 30^\circ$  latitude where one would be more sensitive to the deep abundances of volatiles.

Another issue is whether temperatures are systematically different at hot spots, as indicators of dynamic activity. Examination of the zonal mean properties of Jupiter's atmosphere has established a general anti-correlation between the dark, visible belts and the '(bright', warm zonal thermal structure (e.g. Gierasch *et al.* 1986). This general anticorrelation also extends to the  $5\text{-}\mu\text{m}$  structure in the zonal average, as well. On the other hand, any relationship between the zonal variability of tropospheric temperatures and  $5\text{-}\mu\text{m}$  radiances, if there is one, remains to be established. Whether both are related to some sort of wave phenomena is the most compelling possibility. Examination of the longitudinal tropospheric temperature scan at the PES latitude, Figs. 13 and 14, show that considerable longitudinal structure is seen in all three epochs and both pressure levels. On the other hand, no clear, single wavenumbers are evident. The predominant wavenumbers observed in the  $5\text{-}\mu\text{m}$  data are wavenumbers 8, 9, and 10 (Ortiz *et al.* 1997). They report a strong wavenumber 10 for their January-December, 1995, data and a strong wavenumber 8 with a weaker wavenumber 9 feature for the January-September, 1996 period. At the 250-mbar and 316-mbar levels, Figs. 15 and 16, we find no significant peaks in the range 8-10 for November, 1995. For December, 1995 we do find a weak wavenumber 10 peak at the 316-mbar level, like Ortiz *et al.* 1997, but without any analogous peak at the 250-mbar level. Contrasting this, the wavenumber-8 feature shows up only at the 250-mbar level for December, 1995, and not the 316-mbar level. In agreement with Ortiz *et al.* 1997, the January, 1996 data do show a wavenumber-8 feature. However, the wavenumber-8 feature is not pure, and considerable power is present in many other wavenumbers. The disparity in the rotation rates between the tropospheric thermal features and the  $5\text{-}\mu\text{m}$  hot spots and the very narrow confinement of the  $5\text{-}\mu\text{m}$  hot spots does not suggest a common origin.

Deming *et al.* (1997) have suggested that the tropospheric thermal structures may be manifestations of vertically propagating Rossby waves. Our lack of firm rotation rates for the thermal structures prevents a direct comparison with their hypothesis. Instead, here we note the characteristics of the thermal structures as a function of our three epochs and two pressure levels. At both pressure levels, all three epochs show significant features at wavenumbers 3 and 5-6. At other wavenumbers, there are considerable differences between the epochs and the two pressure levels. The 1995 December data at the 316-mbar level show peaks at wavenumbers of 10-12 and 15 with no similar structures seen at the 250-mbar level. Contrasting this are the wavenumber 11 and 17 peaks seen at both pressure levels in the 1996 January data. Since our tropospheric temperature retrievals were limited to two levels, we cannot establish a trend with depth of the wavenumber spectrum.

Focusing on the 250-mbar level, the December, 1995 and January, 1996 spectra have a peak at wavenumber 8 while the November, 1995 data do not. Interpretations of these changes must be reconciled with the lack of clear-period features and the longitudinal gaps, particularly for November, 1995. It is possible that the structures responsible for the wavenumber-8 feature are present only in the longitudes sampled in December, 1995, and January, 1996, but not November, 1995. This contrasts with the 316-mbar spectrum where only January, 1996, shows a significant wavenumber-8 peak. Even within these limitations there is considerable change in the wavenumber

content of the longitudinal profiles between the three epochs of observation.

There seems to be no predictability in time or pressure. Some wavenumber peaks are stable from epoch to epoch, but only at a single pressure. Some of the epochs, like January, 1996, show a large degree of similarity between the two pressure levels while others, like December, 1995, are very different at the two pressure levels. Clearly, more analysis of these phenomena over longer and shorter time scales is needed as well as accounting for cloud effects.

Our stratospheric maps have much lower signal-to-noise than our tropospheric maps. Consequently, we extracted longitudinal scans at the PES latitude but did not complete a wave analysis. Examining the longitudinal scans, Fig. 18, the combination of relatively low signal-to-noise and apparent evolution of the longitudinal structure leads to no obvious correlations from epoch to epoch. Orton *et al.* (1994) tentatively identified the rotation rates of the stratospheric features as the same as those of tropospheric temperature features. While the eye can find possible correlations using  $-5.5 \text{ msec}^{-1}$  (Orton *et al.* 1994), the correlations are not robust. Thus we do not at this time assign a rotation rate to the longitudinal structure. Without a well defined rotation rate, we are unable to associate or dissociate the stratospheric structures from the  $5\text{-}\mu\text{m}$  hot spots in general or the PES hot spot specifically.

It is clear that much remains to be done in correlating the zonal wave structure appearing in our data with the vertical waves seen in the lower stratosphere and upper troposphere of the Atmospheric Structure Instrument (ASI) results (*e.g.* Fig. 3 of Stiff *et al.* 1997). It is tempting, for example, to interpret the opposite signs of the thermal waves near the  $5^\circ$  longitude of the PES at the 250- and 316-mbar levels (Fig. 13 and 14) as a zonal manifestation of the waves seen at this level in their plot of vertical temperature structure. However, such a comparison should be done in the context of a model of the upward-propagating wave, coupled with a radiative transfer simulation of the outgoing radiation which can determine whether such waves are detectable over the vertical height of the weighting function.

This is also true of the stratosphere. While it is tempting, on inspection of the 20-mbar local peak of the temperature profile (Fig. 3 of Stiff *et al.* 1997), to assume that it likely corresponds to a peak of 10-mbar equatorial temperatures, our observations show that the opposite is true. Again, a thorough simulation of the upwelling  $7\text{-}\mu\text{m}$   $\text{CH}_4$  emission from the stratosphere must be done to determine the likelihood that the vertical wave structure that we see is associated with the QQQ mechanism proposed by Leovy *et al.* (1991). A model is also required to determine whether these waves are connected to the tropospheric waves and to elucidate whether, for example, the Rossby-waves of the hypothesis for the NEB hot spots of Ortiz *et al.* (1997) could be related to the vertically propagating waves needed by model of Deming *et al.* (1997).

#### ACKNOWLEDGEMENTS

We thank the staff of the NASA Infrared Telescope Facility for their tireless support, with special thanks to telescope operators David Griep, William Golisch, and Charles Kaminski for making many of the service observations, together with John Spencer and John Stansberry for making additional observations of Jupiter during their own intensive runs. We are also grateful to the support of William Hoffmann, Aditya Dayal, and Joseph Hera for the use of and help in operating the MIRAC2 instrument, and to Michael Ressler for the use of and help in operating the MIRLIN instrument. Several others helped during observing runs, including A. James Friedson, Padma Yanamandra-Fisher and Jay Goguen. We are grateful for help and useful conversations with Reta Beebe, Nancy Chanover, Jim Friedson, Kathy Rages, Amy Simon, John Trauger, and Robert West. Carol Lachata at the JPL Photography Group deserves special thanks for her preparation

of the color graphics in their final form. This work was supported by the Galileo mission, by the Space Telescope Science Institute which is operated by the Association of Universities for Research in Astronomy, and by research grants from NASA's Planetary Atmospheres discipline to the Jet Propulsion Laboratory, California Institute of Technology,



## REFERENCES

- Atreya, S. K. Atmospheres and Ionospheres of the Outer Planets and Their Satellites. Springer-Verlag, New York and Berlin, 1986.
- Atreya, S. K. and P. NT. Romani. in Planetary Meteorology (G. E. Hunt, ed. ) Cambridge Univ. Press, 17-68, 1985.
- Baines, K., et al. Quasi-Random Narrow-Band Model Fits to Near-Infrared Low-Temperature Laboratory Methane Spectra and Derived Exponential-Sum Absorption Coefficients. *J. Geophys. Res.*, 98, 5517-5529, 1993.
- Banfield, D., et al. 2  $\mu$ m Spectrophotometry of Jovian Stratospheric Aerosols - Scattering Opacities, Vertical Distributions, and Wind Speeds. *Icarus*, 121, 389-410, 1996.
- G. Birnbaum, A. Borysow, and G. S. Orton. Collision-induced absorption of H<sub>2</sub>-H<sub>2</sub> and H<sub>2</sub>-He in the rotational and fundamental band for planetary applications. *Icarus* 123, 4 - 22, 1996.
- Bjoraker, G. L, H. P. Larson, and V. G. Kunde. The abundance and distribution of water vapor in Jupiter's atmosphere. *Astrophys. J.* 311, 1058-1072, 1986..
- Carlson, B. E., W. B. Rossow, and S. G. Orton. Cloud microphysics of the giant planets. *J. Atmospheric Sci.* 45, 2055-2081, 1988.
- Chahine, M. T. inverse problems in radiative transfer: Determination of atmospheric parameters. *J. Atmos. Sci.* 27', 960-967, 1970.
- Chanover, N. J., Kuehn, D.M., Banfield, D., Momary, T., Beebe, R. F., Baines, K.H., Nicholson, I'.1.), Simon, A. A., Murrell, A.S. Absolute Reflectivity Spectra of Jupiter: 0.253.5 Micrometers, *Icarus* 121, 351-360, 1996.
- Chanover, N. J., Kuehn, D.M., Beebe, R.F. Vertical Structure of Jupiter's Atmosphere at the Galileo Probe Entry Latitude. *Icarus*, in press, 1997.
- Collard, A.D., L. A. Sromovsky, G. J., Bjoraker, G.S. Orton. The Deep Jovian Water Abundance from Remote and in Situ Observations. *B.A.A.S.*, 29, 1006, 1997.
- DelGenio, A. D. Moist convection and the vertical structure and water abundance of Jupiter's atmosphere, *Icarus* 84, 29-53, 1990.
- Deming, D., M.J. Mumma, F. Espenak, D. Jennings, T. Kostiuik, G. Wiedemann, R. Loewenstein, J. Piscitelli. A search for p-Mode Oscillations of Jupiter: Serendipitous Observations of Nonacoustic Thermal Wave Structure. *Astrophys. J.* 343, 456-467, 1989.
- Deming, D., D. Reuter, D. Jennings, G. Bjoraker, G. McCabe, K. Fast, G. Wiedemann. Observations and Analysis of Longitudinal Thermal Waves on Jupiter. *Icarus* 126, 301-312, 1997.
- Hoffmann, W. F., G. G. Fazio, K. Shivanandan, J. I., Hera and I., K. Deutsch. MIRAC, a Mid infrared Array Camera for Astronomy. In *Infrared Detectors and Instrumentation*, Ed. A. M. Fowler, *Proc. SPIE* 1946, 449, 1-993.
- Irwin, P. G. J., A. L. Weir, S. Smith, F. W. Taylor, A. L. Lambert, S. B. Calcutt, R. W. Carlson, K. Baines, P. Drossart, Th. Encrenaz, M. Roos-Serote. Cloud structure and atmospheric composition of Jupiter retrieved from Galileo NIMS Real-time Spectra *J. Geophys. Res.*, 1997.
- Magalhaes, J. A., A. L. Weir, P. J. Gierasch, B. J. Conrath, S. S. Leroy. *Nature* 337, 444-447, 1989
- Magalhaes, J. A., A. L. Weir, P. J. Gierasch, B. J. Conrath, S. S. Leroy. Zonal motion and structure in Jupiter's upper troposphere from Voyager infrared and imaging observations. *Icarus* 88, 39-72, 1990.
- Gierasch, P. J., J. A. Magalhaes, and B. J. Conrath. Zonal mean properties of Jupiter's upper troposphere from Voyager infrared observations. *Icarus* 67, 456-483, 1986.

Ortiz, J. L., G. S. Orton, S. T. Stewart, B.M. Fisher. Time Evolution and Longitudinal Persistence of 5-pin Hot Spots at the Galileo Probe Entry Latitude. *J.Geophys.Res.*, 1997.

Orton, G. S., A. J. Friedson, J. Caldwell, H. H. Hammel, K. H. Baines, J. P. Bergstralh, T. Z. Martin, M. E. Malcom, R. A. West, A. T. Tokunaga, D. M. Griep, W. F. Golisch, C. D. Kaminsky, R. Baron and M. Shure. Thermal maps of Jupiter: Spatial organization and time dependence of stratospheric temperatures, 1980-1991. *Science* 252, 537-542, 1991.

Orton, G., A.J. Friedson, P.A. Yanamandra-Fisher, J. Caldwell, H.B. Hammel, K.H. Baines, J. P. Bergstralh, T.Z. Martin, R.A. West, G.J. Veeder Jr., D.K. Lynch, R. Russel, M.E. Malcolm, W.F. Golisch, D.M. Griep, C.D. Kaminski, A.T. Tokunaga, J. Herbst, M. Shure. Spatial Organization and Time Dependence of Jupiter's Tropospheric Temperatures, 1980-1993. *Science* 265, 625-631, 1994.

Orton, G., M. A'Hearn, K. Baines, D. Deming, J. Dowling, J. Goguen, C. Griffith, H. Hammel, W. Hoffmann, D. Hunten, D. Jewitt, T. Kostiuik, S. Miller, K. Nell, K. Zahnle, N. Achillesos, A. Dayal, I. Deutsch, F. Espenak, P. Esterle, J. Friedson, K. Fast, J. Harrington, J. Hora, R. Joseph, D. Kelly, R. Knacke, J. Lacy, C. Lisse, J. Rayner, A. Sprague, M. Shure, K. Wells, P. Yanamandra-Fisher, D. Zipoy, G. Bjoraker, D. Buhl, W. Golisch, D. Griep, C. Kaminski, C. Arden, A. Chaikin, J. Goldstein, D. Gilmore, G. Fazio, T. Kanamori, H. Lam, T. Livengood, M.-M. MacLow, M. Marley, T. Momary, D. Robertson, I. Romani, J. Spitale, M. Sykes, J. Tennyson, D. Wellnitz, and S.-W. Ying. The NASA Infrared Telescope Facility investigation of Comet Shoemaker-Levy 9 and its collision with Jupiter. *Science* 267, 1277 - 1282, 1995.

Orton, G., J. L. Ortiz, K. Baines, G. Bjoraker, U. Carsenty, F. Colas, D. Deming, P. Drossart, E. Frappa, J. Friedson, J. Goguen, W. Golisch, D. Griep, C. Hernandez, W. Hoffmann, D. Jennings, C. Kaminski, J. Kuhn, J. Laques, S. Limaye, H. Lin, J. Lecacheux, T. Martin, G. McCabe, J. Momary, D. Parker, R. Puetter, M. Ressler, G. Reyes, P. Sada, J. Spencer, J. Spitale, S. Stewart, J. Varsik, J. Warell, W. Wild, P. Yanamandra-Fisher, A. Dayal, I. Deutsch, G. Fazio, and J. Hera. Preliminary Results of Earth-Based Observations of the Galileo Probe Entry Site. *Science* 272, 839 - 840, 1996.

Orton, G., T. Martin, J. Tamppari, O. Liepack, B. Fisher, J. Friedson, M. Ressler, R. Yanamandra-Fisher, K. Baines, R. West, I. Travis, S. Stewart, H. Peiris, E. Noe Dobrea, S. Hinkley, W. Golisch, D. Griep, and C. Kaminski. Atmospheric structure of Jupiter from radiometric observations of the Galileo Photopolarimeter-Radiometer (PPR) and ancillary earth-based observations. *Bull Amer. Astron. Soc.* 29, 1005, 1997.

Press, W. H., W.T. Vetterling, B.F. Flannery. *Numerical Recipes in C*, Cambridge University Press, New York, New York, 1992.

Rayner, J., M. Shure, D.W. Toomey, P. Onaka, A. Denault, W. Stahlberger, D. Watanabe, K. Criez, L. Robertson, D. Cook and M. Kidger. *SPIE* 1946, 490, 1993.

Ressler, M. E., M. W. Werner, J. Van Cleve, J., and H. A. Chou. The JPL Deep-Well Infrared Array Camera". In *Infrared Astronomy with Arrays: The Next Generation*, Ed. Ian McLean, *Experimental Astronomy*, 3, 277, 1994.

Rogers, J. H. The giant planet Jupiter. Cambridge University Press, Cambridge, UK, 1995.

Roos-Serote, M., P. Drossart, Th. Encrenaz, E. Lellouch, R. W. Carlson, K. H. Baines, I. Kamp, R. Mehlman, and G. Orton, S. Calcutt, P. Irwin, F. Taylor and A. Weir. Analysis of Jupiter NEB hot spots in the 4- 5  $\mu\text{m}$  range from Galileo/NIMS observations: measurements of water, ammonia and cloud opacity. *J. Geophys. Res.*, 1997.

Sciff, A., D. B. Kirk, T. C.D. Knight, I. A. Young, F. S. Miles, E. Venkatapathy, J. D. Mihalov,

R.C. Blanchard, R. E. Young, and G. Schubert. Thermal structure of Jupiter's upper atmosphere derived from the Galileo Probe. *Science* 276, 102-104.

Smith, P. H. and M. G. Tomasko. Photometry and polarimetry of Jupiter at large phase angles. 11- Polarimetry of the south tropical zone, south equatorial belt, and the polar regions from the Pioneer 10 and 11 missions. *Icarus* 58, 35-73. 1984.

Sromovsky, L. A., F. A. Best, A. D. Collard, P. M. Fry, H. E. Revercomb, R. S. Freedman, G. Oton, J. Hayden. Preliminary results of the Galileo Net Flux Radiometer Experiment. *Science* 272, 851-854, 1996.

Sromovsky, L. A., A. D. Collard, P. M. Fry, G. S. Orton, M. T. Lemmon, M. G. Tomasko, and R. S. Freedman. Galileo Probe measurements of thermal and solar radiation fluxes in the Jovian atmosphere. *J. Geophys. Res.*, 1997.

Stewart, S. T., G. S. Orton, B. M. Fisher, K. H. Baines. The Cloud Structure of the Jovian North Equatorial Zone: Context of the Galileo Probe Entry Latitude. submitted to *J. Geophys. Res.-Planets*, 1997.

Vasavada, A. R., A. P. Ingersoll, D. Banfield, M. Bell, P. J. Gierasch, and M. J. S. Belton. Galileo imaging of Jupiter's atmosphere: The Great Red Spot, equatorial region, and White Ovals. *Icarus*. Submitted. 1997.

Weidenschilling, S. J. and J. S. Lewis. Atmospheric and cloud structure of the Jovian planets. *Icarus* 20, 465-476, 1973.

West, R. A., D. F. Strobel, M. G. Tomasko. Clouds, Aerosols, and Photochemistry in the Jovian Atmosphere. *Icarus* 65, 161-217, 1986.

West, R. A., E. Karkoschka, A. J. Friedson, M. Seymour, K. H. Baines, H. B. Hammel. Impact debris particles in Jupiter's stratosphere. *Science* 267, 1296-1301, 1995.

## TABLES

Table 1: 11 ST -IRTF coincident observations

HST date	HST time	IR 11' date	IRTF time (UT)	A time (h:m:s)	A longitude (°W)
1995 March 10	20:39:16	1995 March	05:06:30	+ 15:32:46	+ <b>3.19</b>
<b>1996</b> June 27	03:07:16	<b>1996</b> June 26	07:18:18	- 19:48:58	- 4.07

## FIGURE CAPTIONS

Figure 1. History of the  $5\text{-}\mu\text{m}$  hot spot into which the Galileo Probe entered. Each panel is extracted from a cylindrical map created from an image of Jupiter at  $4.78\text{ }\mu\text{m}$  (see Ortiz et al. 1997, this issue). The apparent brightness variations illustrate the observed variations of the absolute radiance of the hot spot, as deduced by Ortiz et al. (1997). The images are centered at  $6.5^\circ\text{N}$  planetocentric latitude, and a longitude moving 99 to 103 m/s faster than the System-I]] rot at ion rate, as described by Ortiz et al. The scale of each panel is  $15^\circ$  latitude by  $29^\circ$  longitude.

Figure 2. Radiance of the Probe entry site  $5\text{-}\mu\text{m}$  hot spot as a function of time. These were measured from the  $4.78\text{-}\mu\text{m}$  images, a subset of which are shown in Figure 1. The lower graph was made with a more restrictive set of criteria relative to the upper graph, as explained in the text.

Figure 3. Comparison of timewise-interpolated  $4.78\text{-}\mu\text{m}$  NSFCAM images of the PES hot spot from outside the time interval when the polypropylene safety screen was required to the 1995 December 7 time of the Galileo Probe entry and the 1996 January 4 follow-up observation. Interpolation was done linearly in time and using the absolutely calibrated images, although the features shown are scaled to the brightest pixel in each panel in the top row. The second level shows interpolated NSFCAM images, convolved with a seeing function that matched images of stars made on 1995 December 7 and 1996 January 4, using the MIRAC2 and MIRELIN instruments, respectively. Both of these sets of data were also made at the IRTF with the polypropylene safety screen. The third level shows the actual observations made by the MIRAC2 and MIRELIN instruments. Because the filter functions are slightly different (MIRAC2 and MIRELIN observing through a slightly broader bandwidth), the MIRAC2 and MIRELIN images were scaled to the relatively constant radiance in the colder Equatorial Zone in the NSFCAM images. The lower panel displays the differences between the actual observations and the convolved and interpolated images on the same absolute brightness scale.

Figure 4. Location of the Probe entry site in the  $5\text{-}\mu\text{m}$  hot spot. The images are taken from the upper panel of Fig. 3 and, again, scaled to the brightest pixel in each image. A single  $1^\circ \times 1^\circ$  pixel is used to denote the  $6.5^\circ\text{N}$  planetocentric latitude of the Probe entry, and a  $1.5^\circ$  longitude ( $3\text{-pixel}$ ) extent depicts the longitudinal extent of the Probe entry path, starting from 350 ktn above the 1-bar level to the 1-bar level and deeper (as in Figs 1 and 2 of Orton *et al.*, 1996).

Figure 5. Comparison of  $4.78\text{-}\mu\text{m}$  radiance measured by NSFCAM at the IRTF with 953-nm and 410-nm radiance measured by the HST Planetary Camera for the 1995 October epoch shown in Table 1. The  $10^\circ$  latitude by  $20^\circ$  longitude region centered on the feature at  $6.5^\circ\text{N}$  planetocentric latitude are shown in the upper two panels. The upper panel is an enhanced color composite taken from cylindrical projections of HST PC images. The panel beneath it is the same region taken from an IRTF NSFCAM  $4.78\text{-}\mu\text{m}$  image. A larger region covered by this image is shown in Fig. 1. The lower two panels show the correlation between the  $4.78\text{-}\mu\text{m}$  thermal radiance and the reflectivity. The HST image has been shifted in longitude to match the motion of the hot spot during the short time separation between the two sets of observations (Table 1). Note that the PES hot spot is in an “early” and geographically small stage of development. The colored curves in the correlation plots are linear regression fits to the data, excluding points with  $4.78\text{-}\mu\text{m}$  radiance less than  $0.06\text{ W/m}^2/\text{ster/mum}$ . The correlation coefficient for the 953-nm *vs.*  $4.78\text{-}\mu\text{m}$  radiance is 0.66 and for the 410-nm *vs.*  $4.78\text{-}\mu\text{m}$  radiance is 0.41, in the negative sense.

Figure 6. Comparison of  $4.78\text{-}\mu\text{m}$  radiance measured by NSFCAM at the IRTF with 953-nm and 410-nm radiance measured by the HST Planetary Camera for the 1996 June epoch shown in Table 1. The panels correspond to their counterparts in Figure 5, except that the HST images are

from the WF instrument. We note that the PES hot spot is in a “mature” phase of development compared with 1995 October. The lower resolution of the NSFCAM image compared with 1995 October is the result of poorer atmospheric seeing conditions. The correlation coefficient for the 953-nm *vs.* 4.78- $\mu$ m radiance is 0.91 and for the 410-nm *vs.* 4.78- $\mu$ m radiance is 0.52, in the negative sense.

Figure 7. Comparison of latitudinal dependence of 953-nm and 410-nm reflectivity, taken from cylindrical projections of HST images from 1995 October, as shown in the upper two panels. The region shown is the same as in Figure 5. The arrow indicates the longitude from which the graph of reflectivity *vs.* latitude is taken in the bottom panel.

Figure 8. Comparison of latitudinal dependence of 953-nm and 410-nm reflectivity, taken from cylindrical projections of HST images from 1996 June, as shown in the upper two panels. The region shown is the same as in Figure 6. The arrow has the same meaning as in Fig. 7.

Figure 9. Comparison of spectral reflectivity of the PES for the various epochs of HST observations. The observed reflectivity has been adjusted to emission and incident angles of  $45^\circ$  each. The reflectivities are taken from exactly  $6.5^\circ$  N planetocentric latitude and a 10 span of longitude centered on the PES (*e.g.* Figs. 5- 8). The error bars represent a combination of the variance of the measured I/F values and the propagation of uncertainties of the Minnaert coefficients used to adjust to a common geometry. Not shown is a  $\sim 5\%$  uncertainty in the absolute calibration affecting all the data. Note that the 893-nm point is influenced by a strong absorption band of gaseous  $\text{CH}_4$ .

Figure 10. Comparison of spectral reflectivity of the PES hot spot center for the various epochs of HST observations. The plot is identical to Fig. 9, except that the latitude from which the data were taken was chosen as that in which the “red” reflectivity was a minimum, *e.g.*  $7.0^\circ$  N in 1995 Oct (Fig. 7) and  $7.5^\circ$  N in 1996 June (Fig. 8).

Figure 11. Comparison of spectral reflectivity the center of another 5- $\mu$ m hot spot some  $40^\circ$  in latitude away from the PES hot spot for the various epochs of HST observations. The plot is otherwise identical to Fig. 10.

Figure 12. Cylindrical projection map of the tropospheric temperature at the 250-mbar pressure level for December, 1995. The PES latitude is at the southern edge of the bright NEB.

Figure 13. Longitudinal temperature profile of the 250-mbar pressure level at  $5-7^\circ$  N. The profile for November 1995 was shifted up by 2 Kelvins and the January 1996 profile was shifted down by 2 Kelvins for clarity. The profiles have been smoothed with sliding  $7^\circ$  boxcar averaging. The error for the temperature retrievals are  $\pm 0.05$  K for November, 1995,  $\pm 0.1$  K for December, 1995, and  $\pm 0.25$  K for January, 1996, as shown by the single error bar at  $20^\circ$  W for each epoch.

Figure 14. Longitudinal temperature profile of the 316-mbar pressure level at  $5-7^\circ$  N. The profile for November 1995 was shifted up by 2 Kelvins and the January 1996 profile was shifted down by 2 Kelvins for clarity. The profiles have been smoothed with sliding  $7^\circ$  boxcar averaging. The error for the temperature retrievals are  $\pm 0.05$  K for November, 1995,  $\pm 0.1$  K for December, 1995, and  $\pm 0.25$  K for January, 1996, as shown by the single error bar at  $20^\circ$  W for each epoch. As expected, the amplitudes of the perturbations decrease with depth.

Figure 15. Lomb normalized periodogram spectrum of the longitudinal structure at  $5-7^\circ$  N at the 250-mbar level.

Figure 16. Lomb normalized periodogram spectrum of the longitudinal structure at  $5-7^\circ$  N at the 316-mbar level.

Figure 17. Cylindrical projection map of the stratospheric brightness temperature derived from 7.8  $\mu$ m data for November, 1995. The bright NEB band showing in the stratosphere starts at a

latitude of approximately  $10^{\circ}$  N, north of the PES latitude. The PES latitude shows no particular structure during this epoch,

Figure 18. Longitudinal scans of the stratospheric brightness temperature derived from  $7.8\ \mu\text{m}$  data averaged over  $50^{\circ}$ – $7^{\circ}$  N for September 5, November 7 (shifted by  $-5\ \text{K}$ ), and December 7 (shifted by  $-10\ \text{K}$ ), 1995. The noise level of the data are shown converted to brightness temperature at the right side of the graph. No clear correlations between the epochs are evident.

Figure 19. Zonal mean meridian scan of the stratospheric brightness temperature derived from  $7.8\ \mu\text{m}$  data for August, 1994 and November, 1995. In November, 1995, the equator has returned to a relatively low state, like that in 1986–1987. The August, 1994 data seems to be intermediate between (i) the warmer mid-latitude / cooler equator state, and (ii) the warmer equator / cooler midlatitude state. The November 1995 state agrees with the quasiquadrennial oscillation hypothesis of Leovy *et al.* (1991).

	1995 Mar 11
	1995 Jul 26
	1995 Aug 11
	1995 Oct 3
	1995 Oct 13
	1995 Nov 21
	1996 Jan 22
	1996 Mar 2
	1996 Jun 26
	1996 Aug 11
	1996 Sep 30
	1996 Nov 20
	1996 Dec 6
	1996 Dec 20
	1997 Feb 20
	1997 Apr 5
	1997 Jul 6
	1997 Aug 5



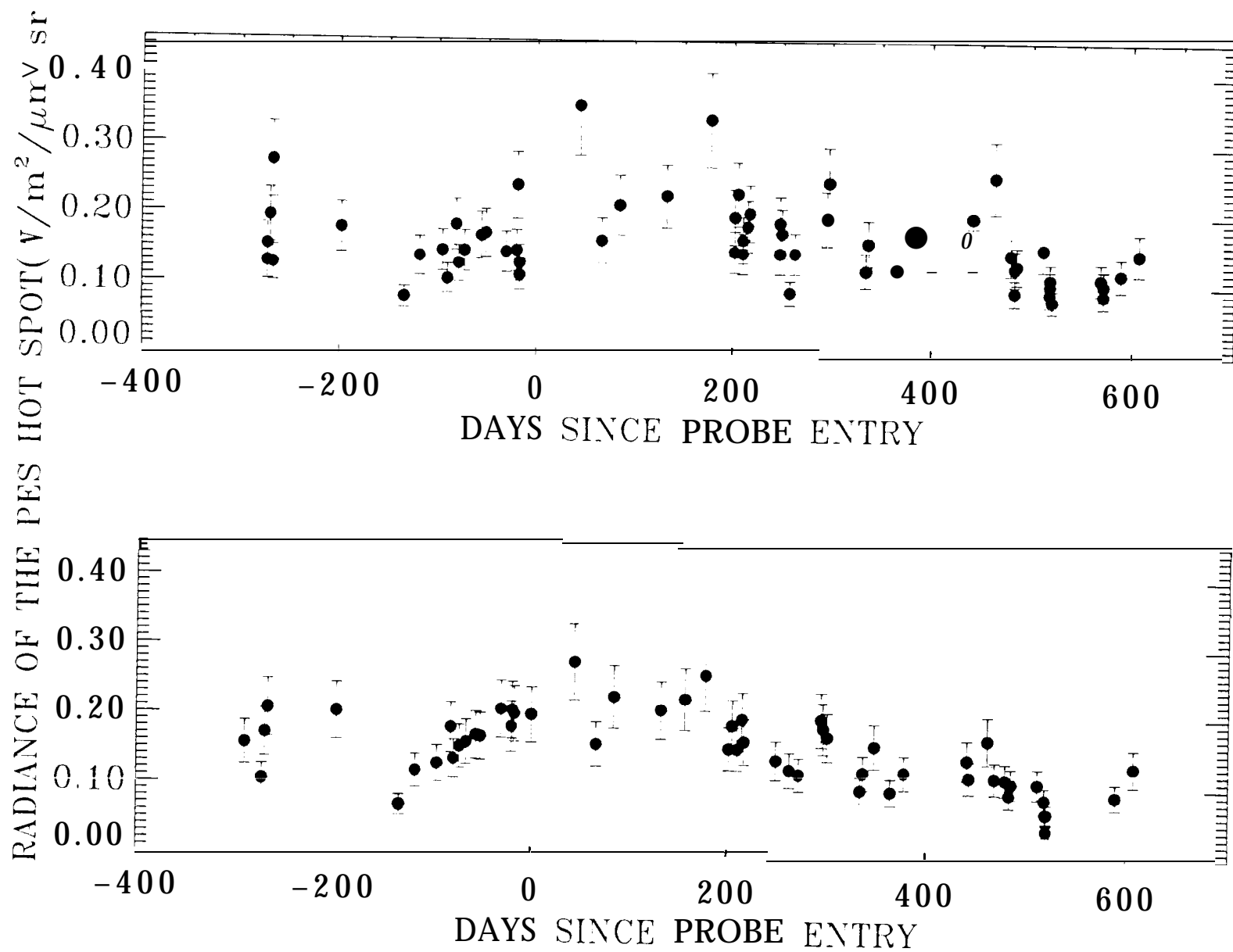


Fig. 2  
u

1995 Nov 21 1995 Dec 7 1996 Jan 4 1996 Jan 22

NSFCAM interpolated NSFCAM



convolved  
and  
interpolated



convolved  
and  
interpolated



MIRAC2



MIRLIN



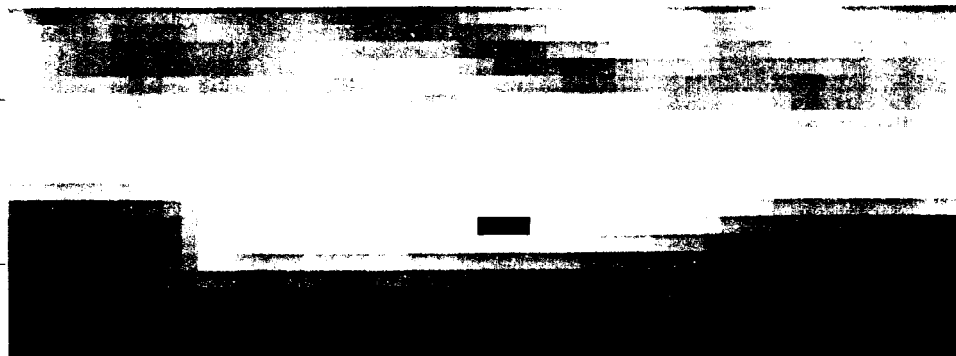
difference

difference

PLANETOCENTRIC LATITUDE (°N)

10—

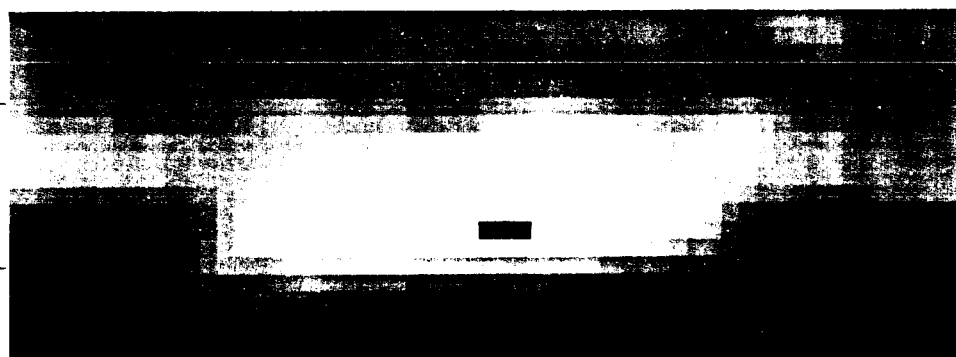
5—



**1995 Nov 21**

10—

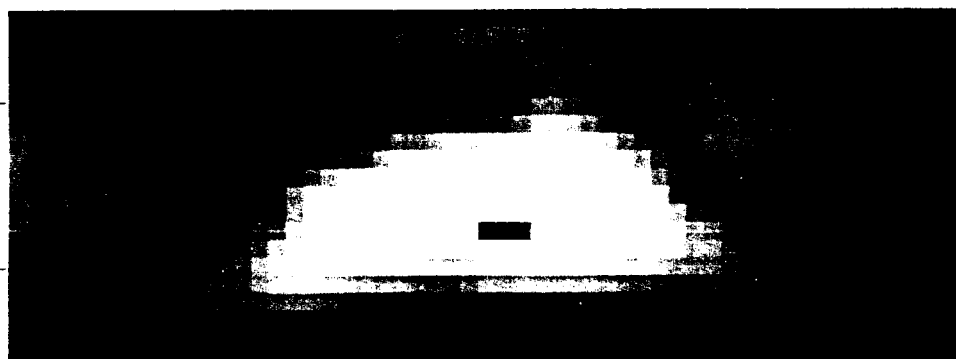
5—



**1995 Dec 7**

10—

5—



**1996 Jan 22**

15

10

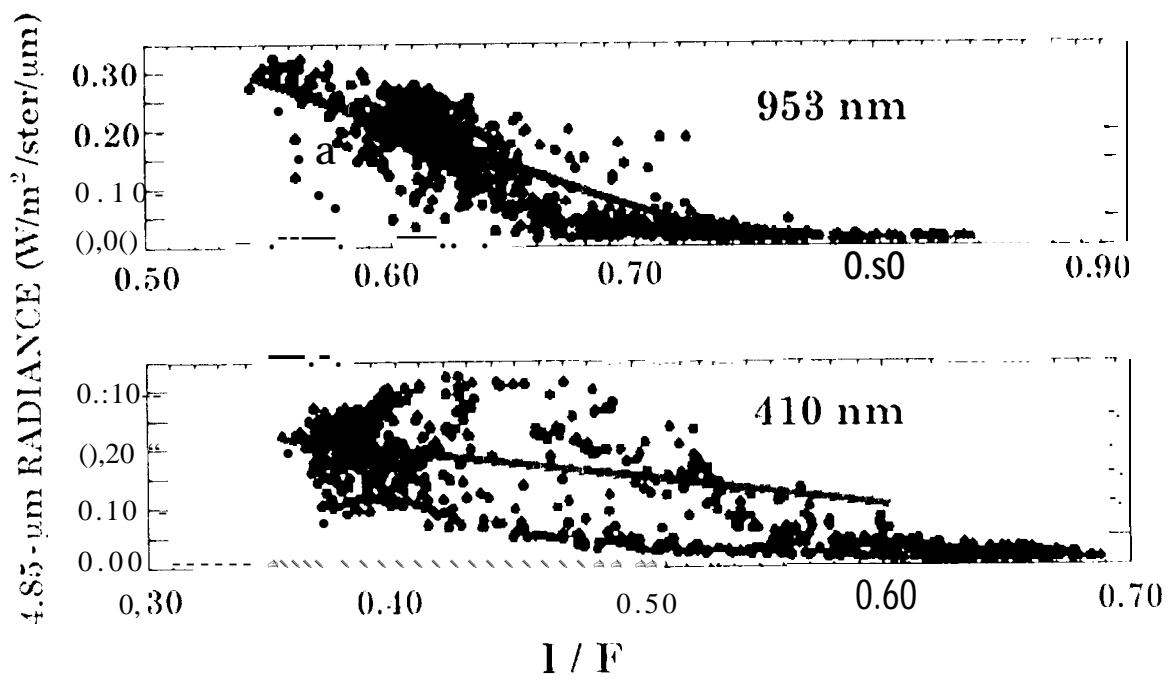
5

0

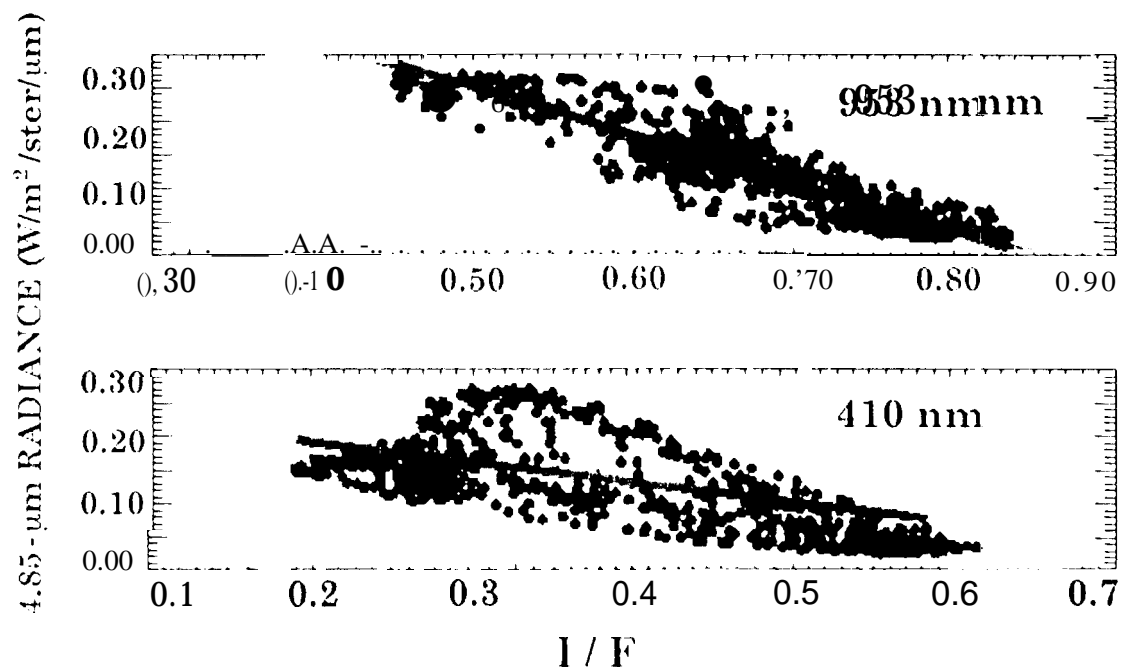
355

LONGITUDE ("W, System III)

1995 October



1996 June

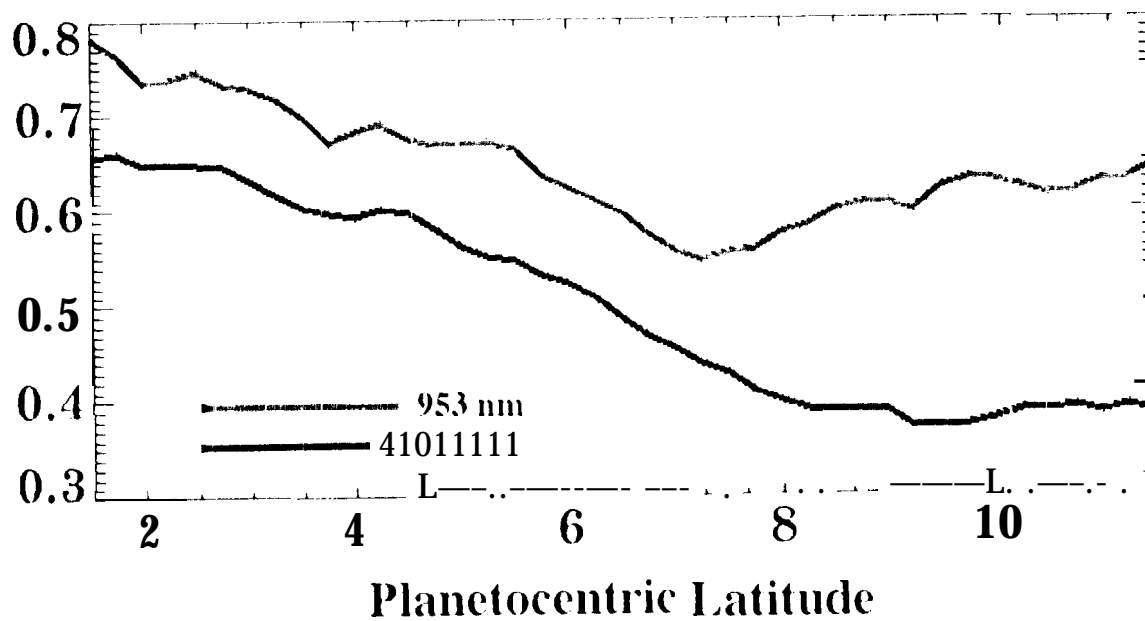




953 nm



410 nm

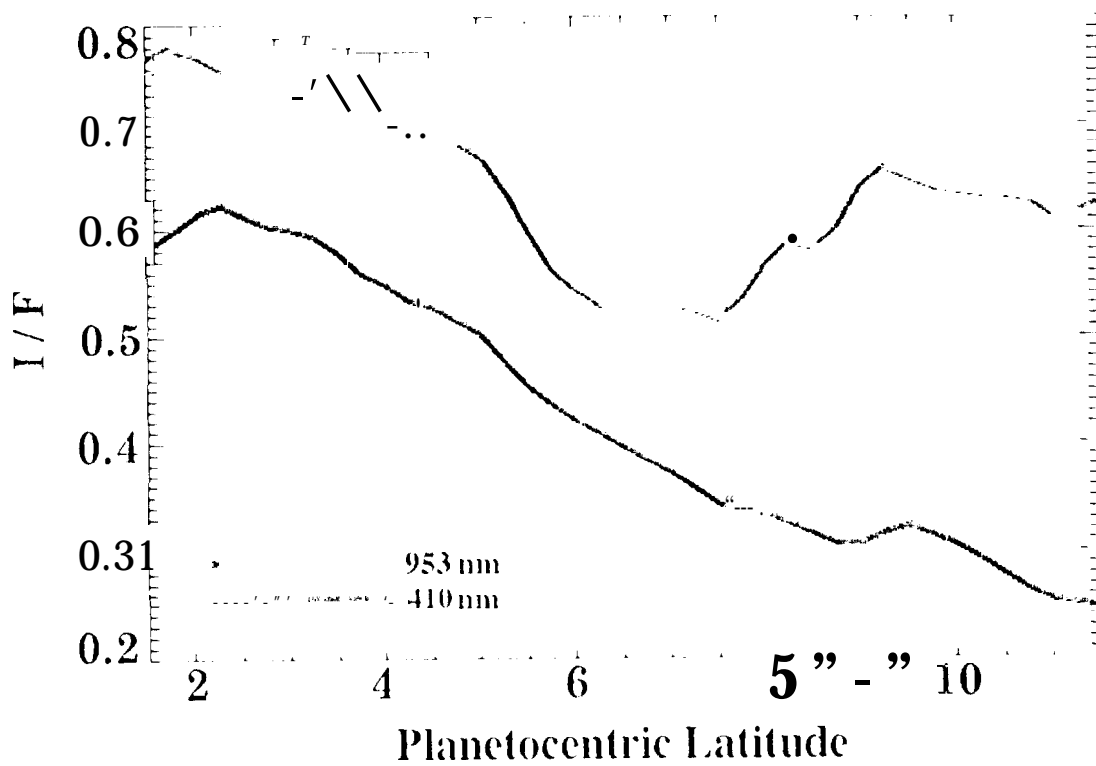


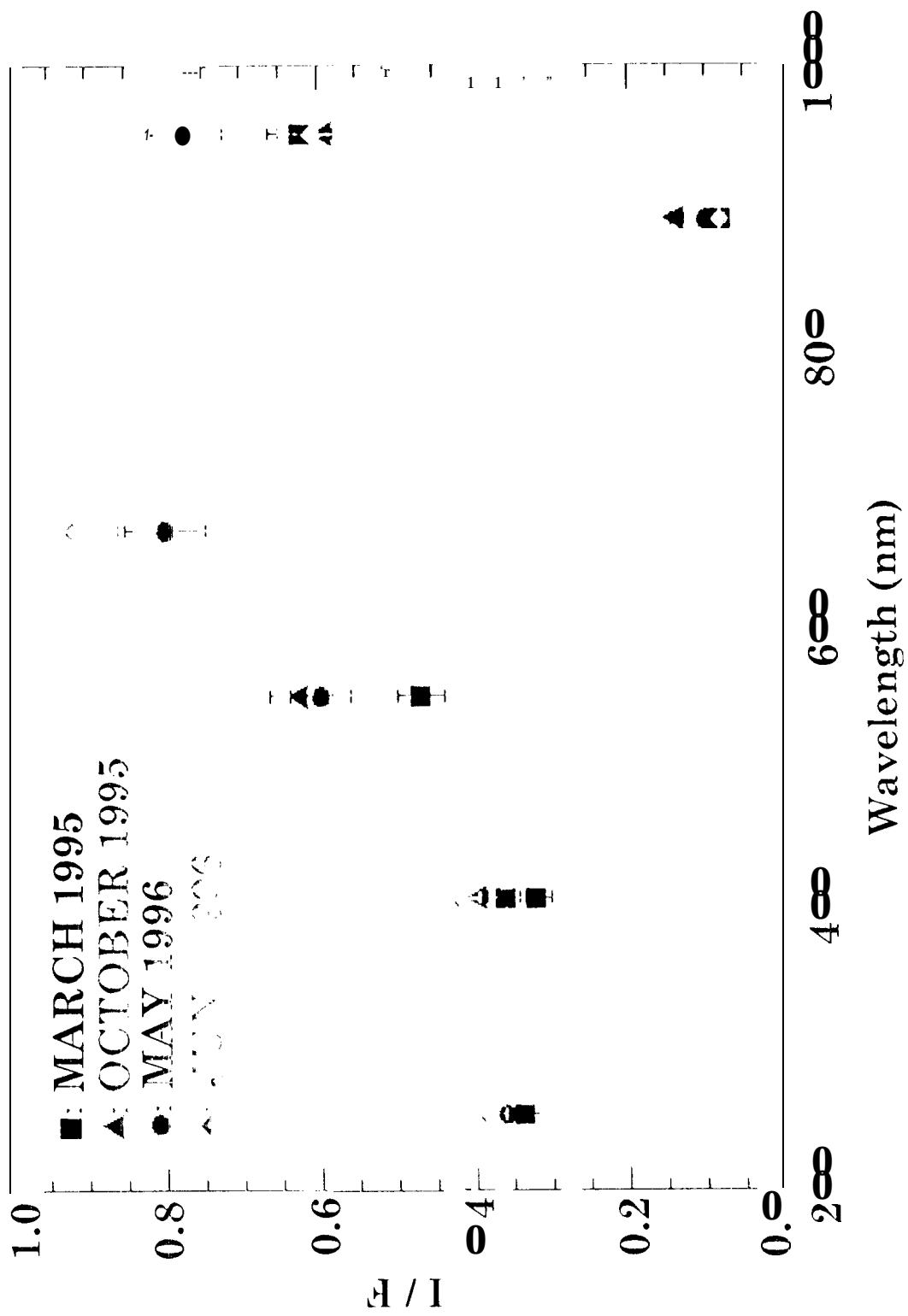


953 nm

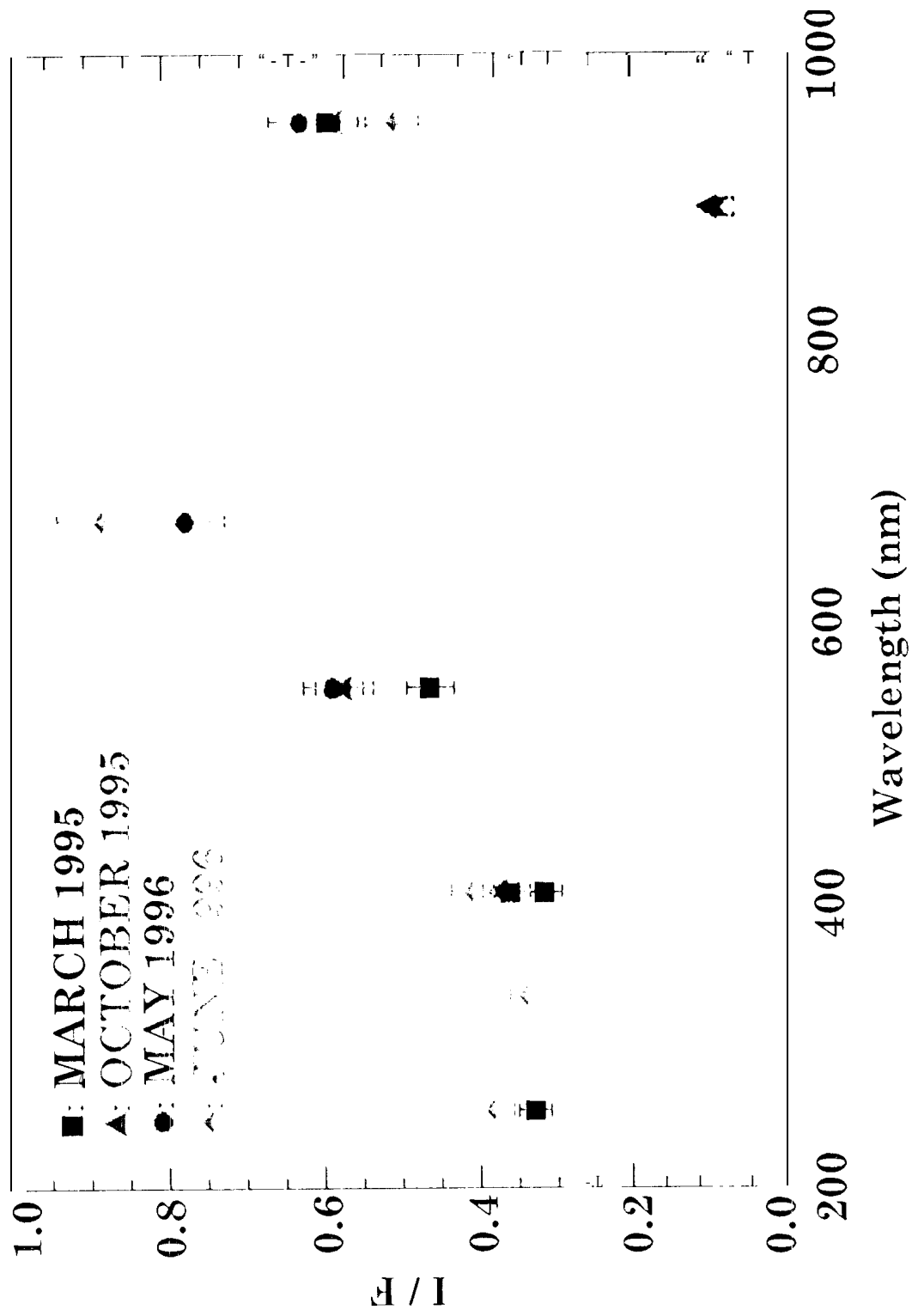


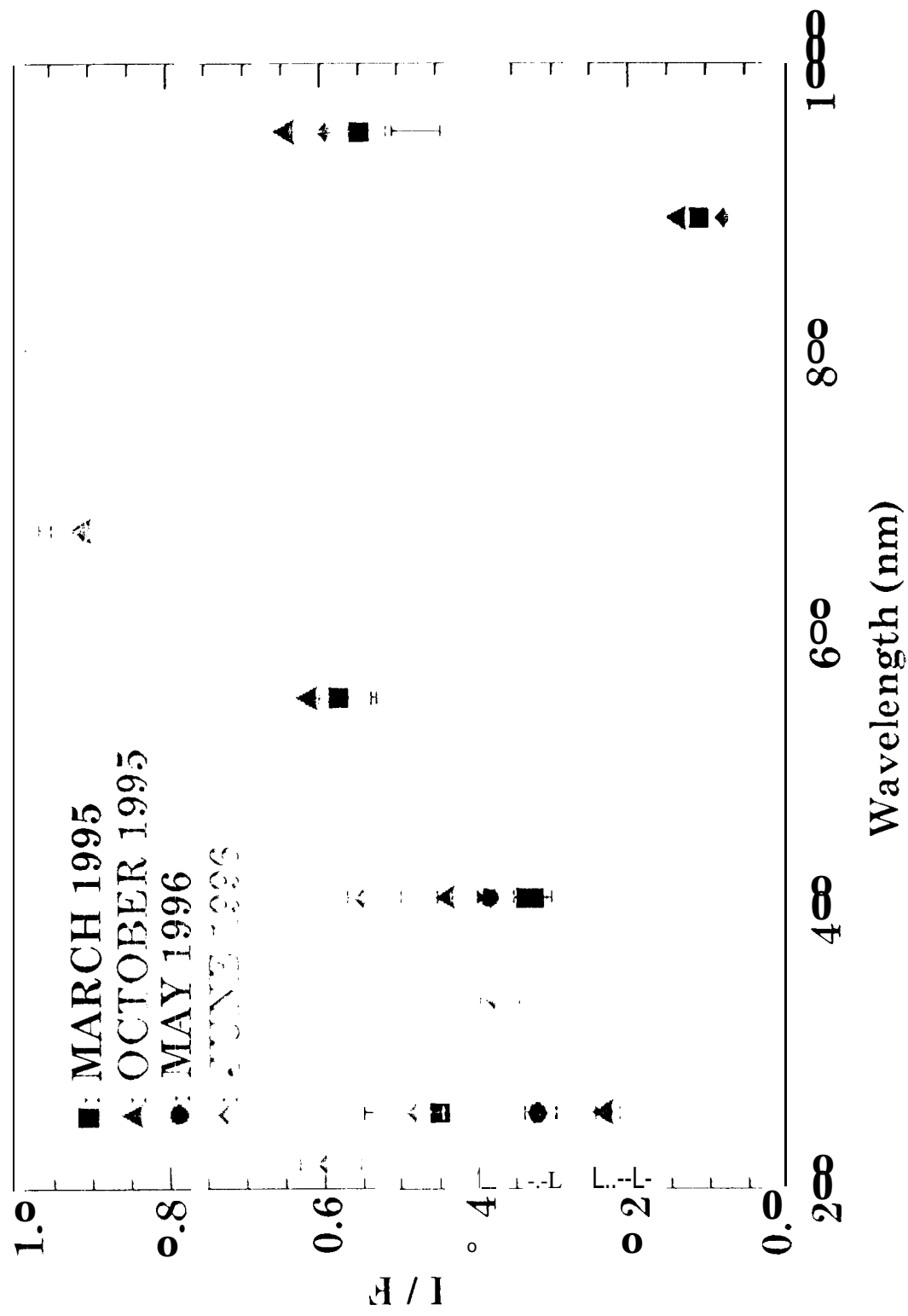
410 nm



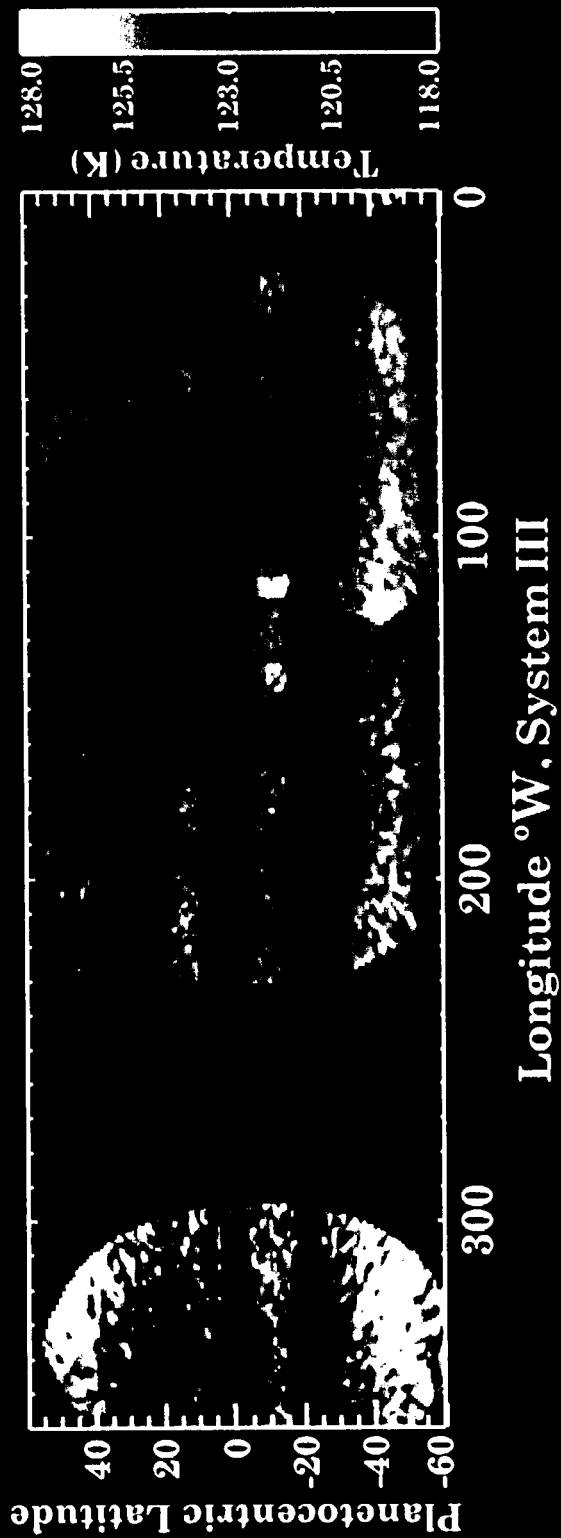


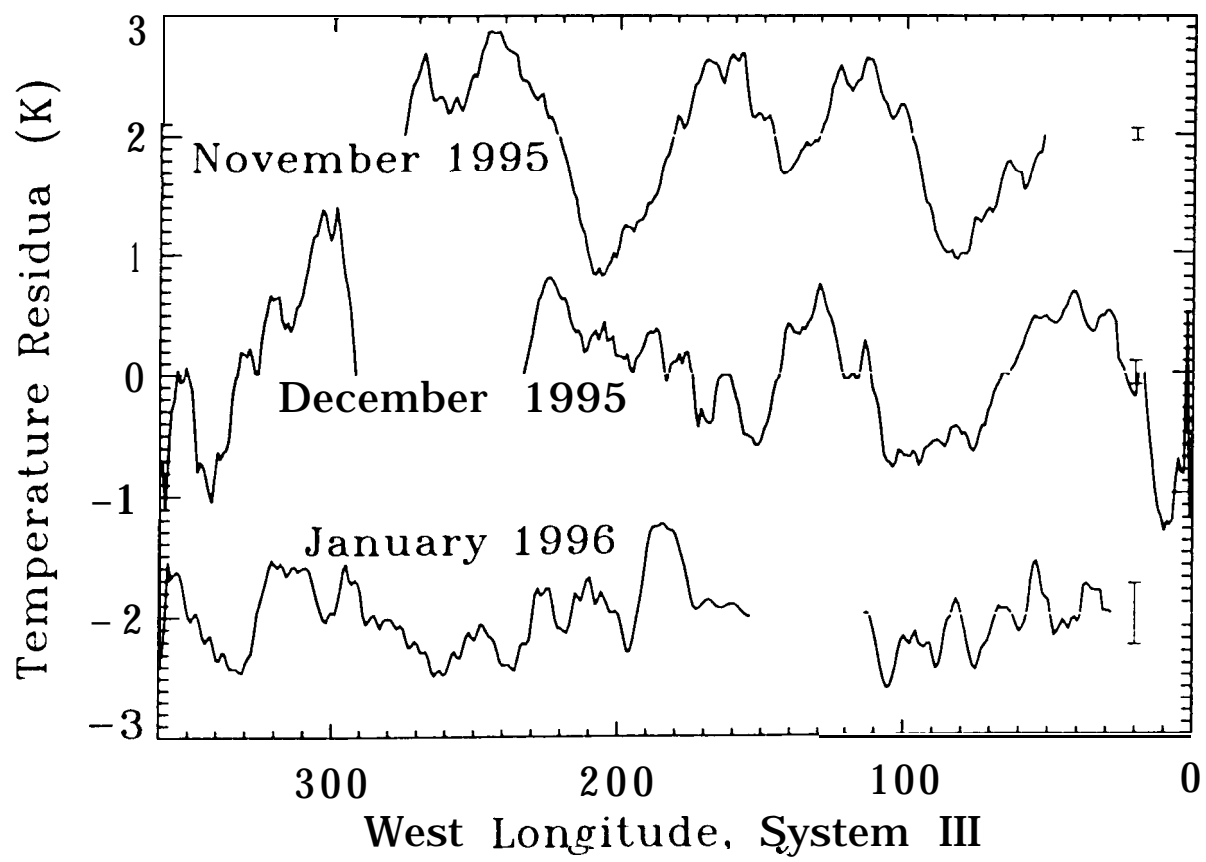






December 1995





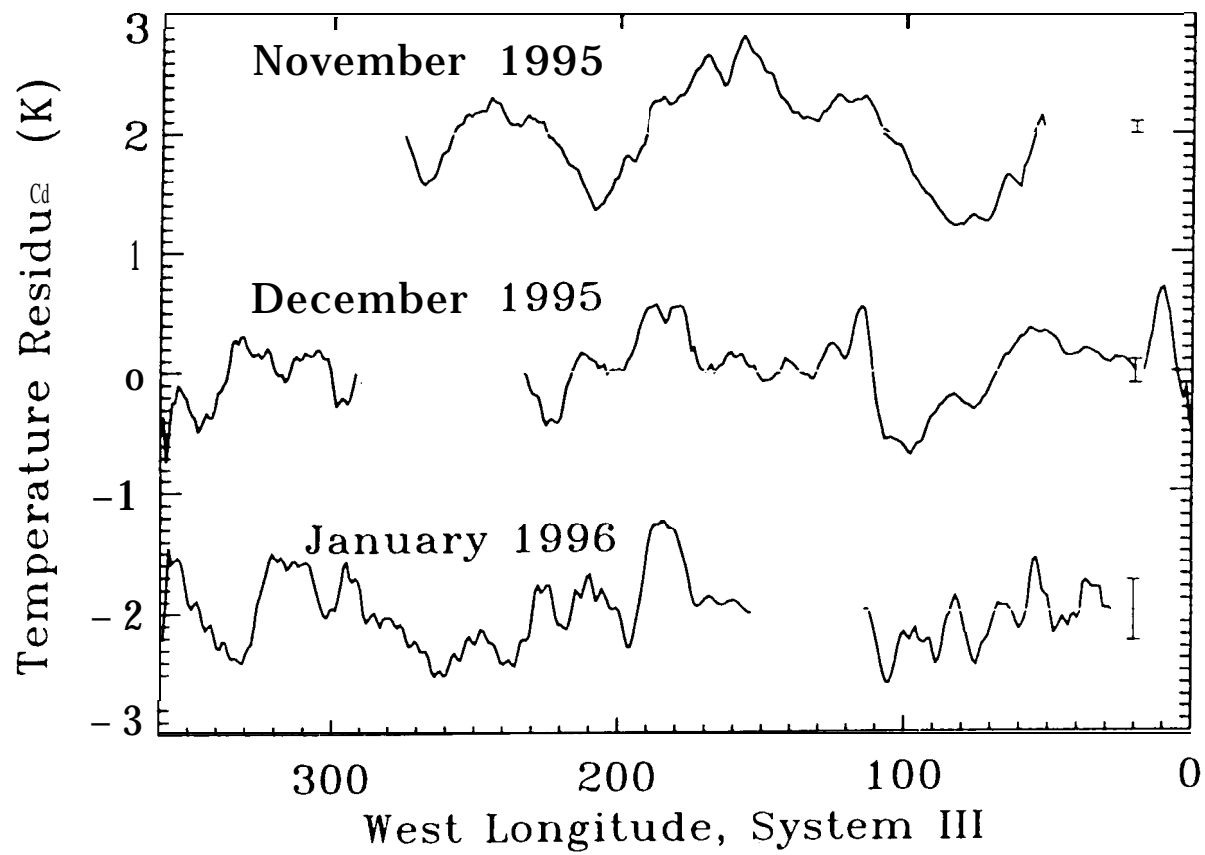
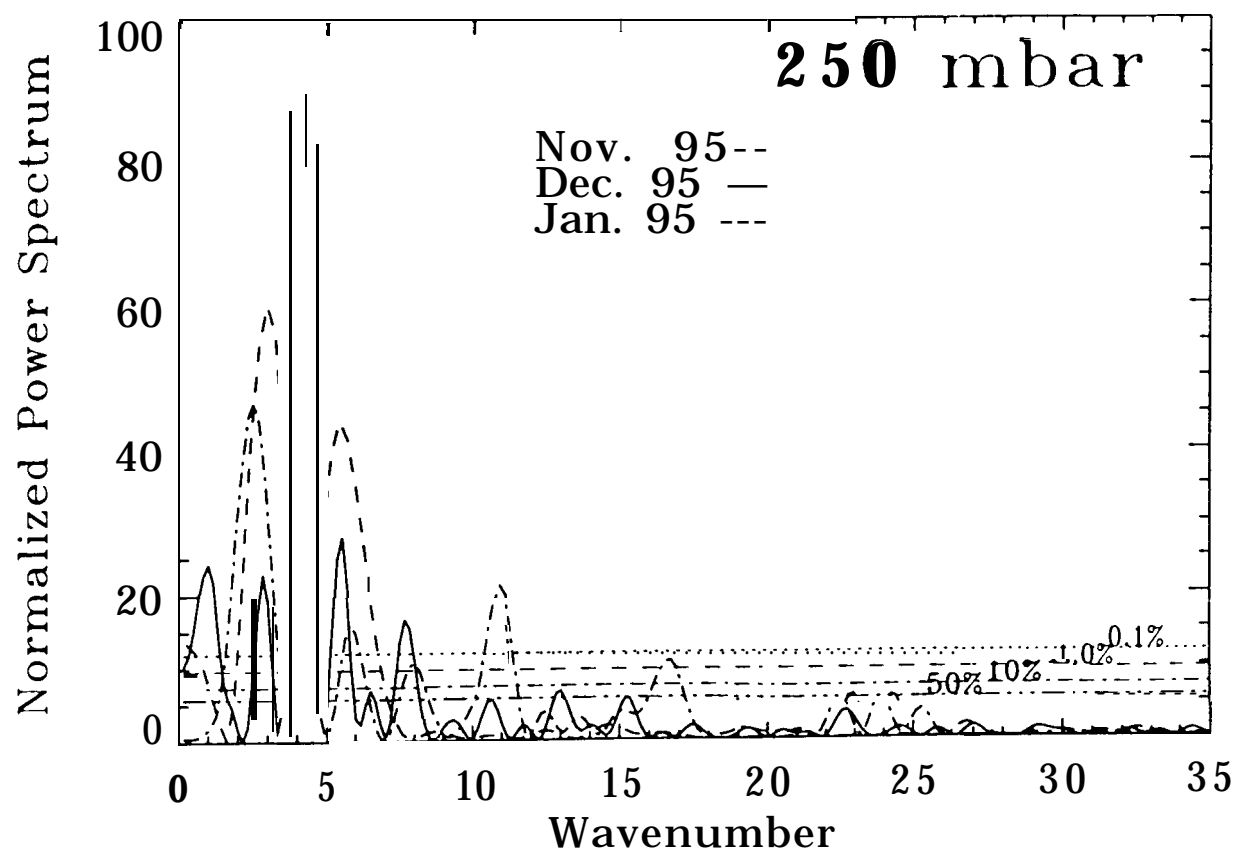


Fig 14



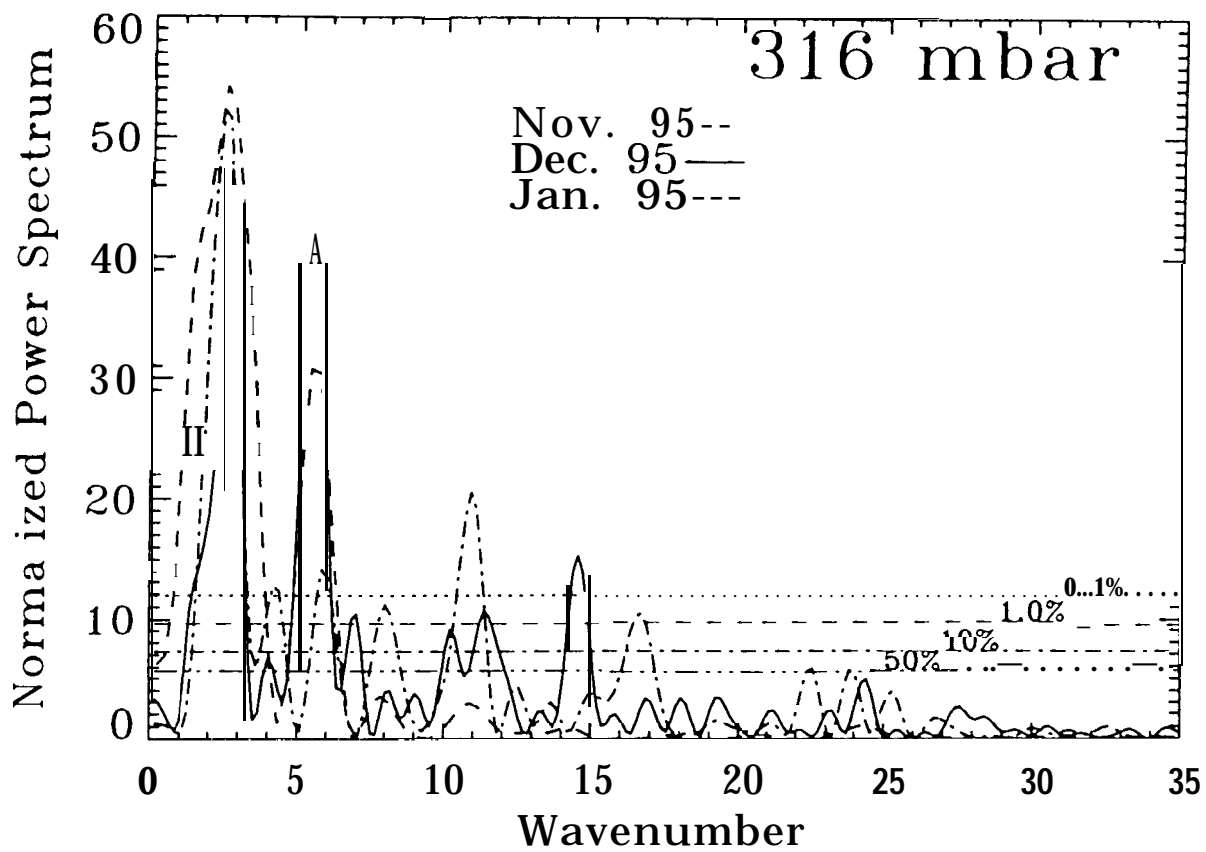
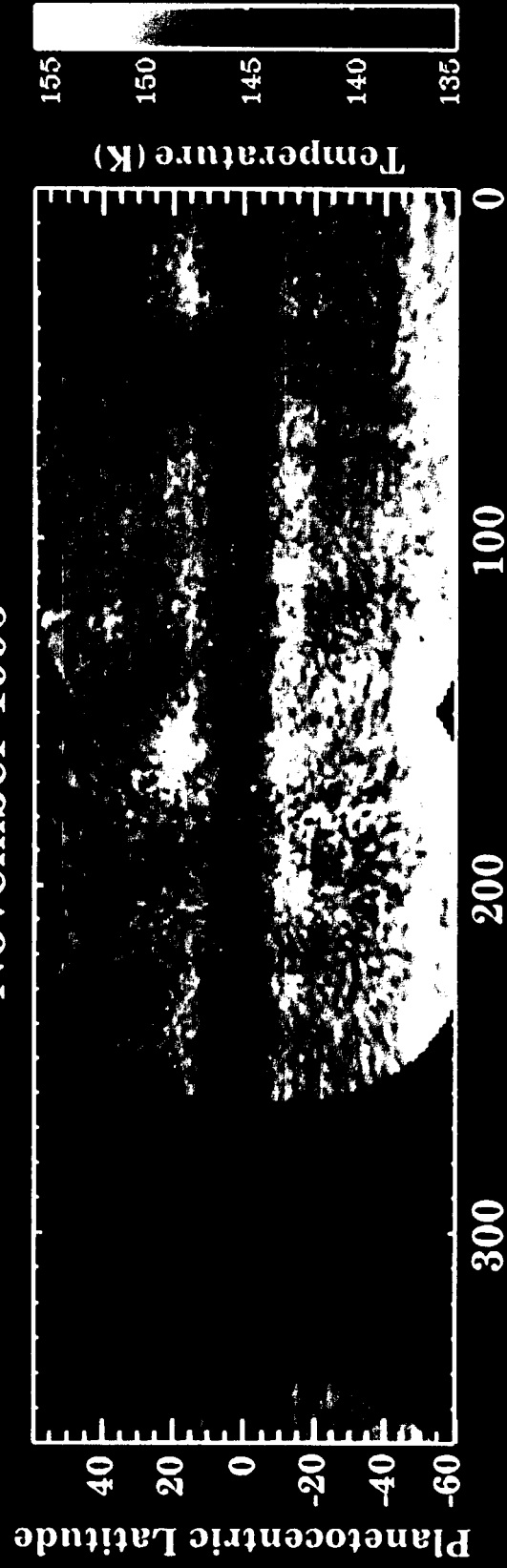
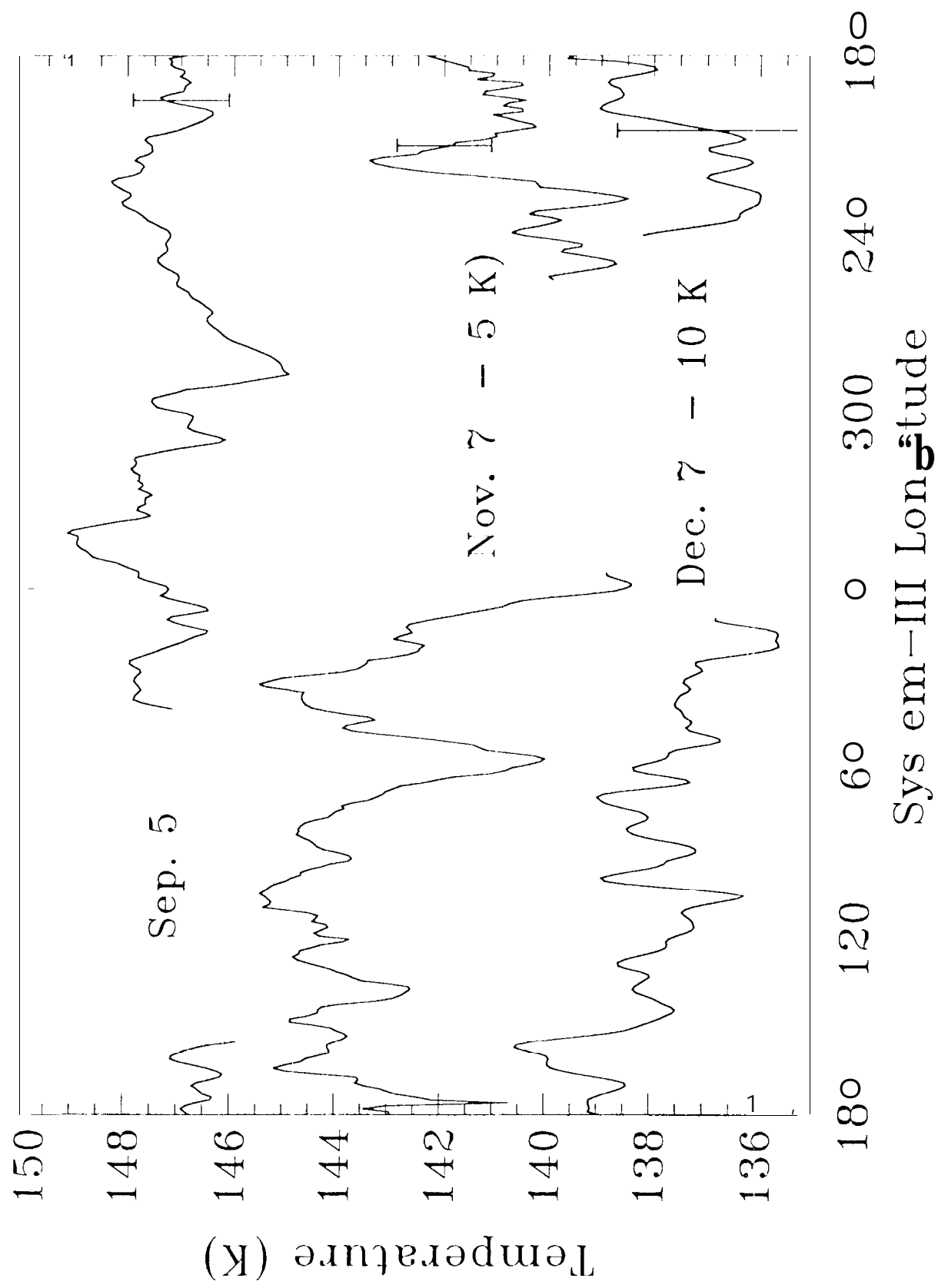


Fig 16

November 1995







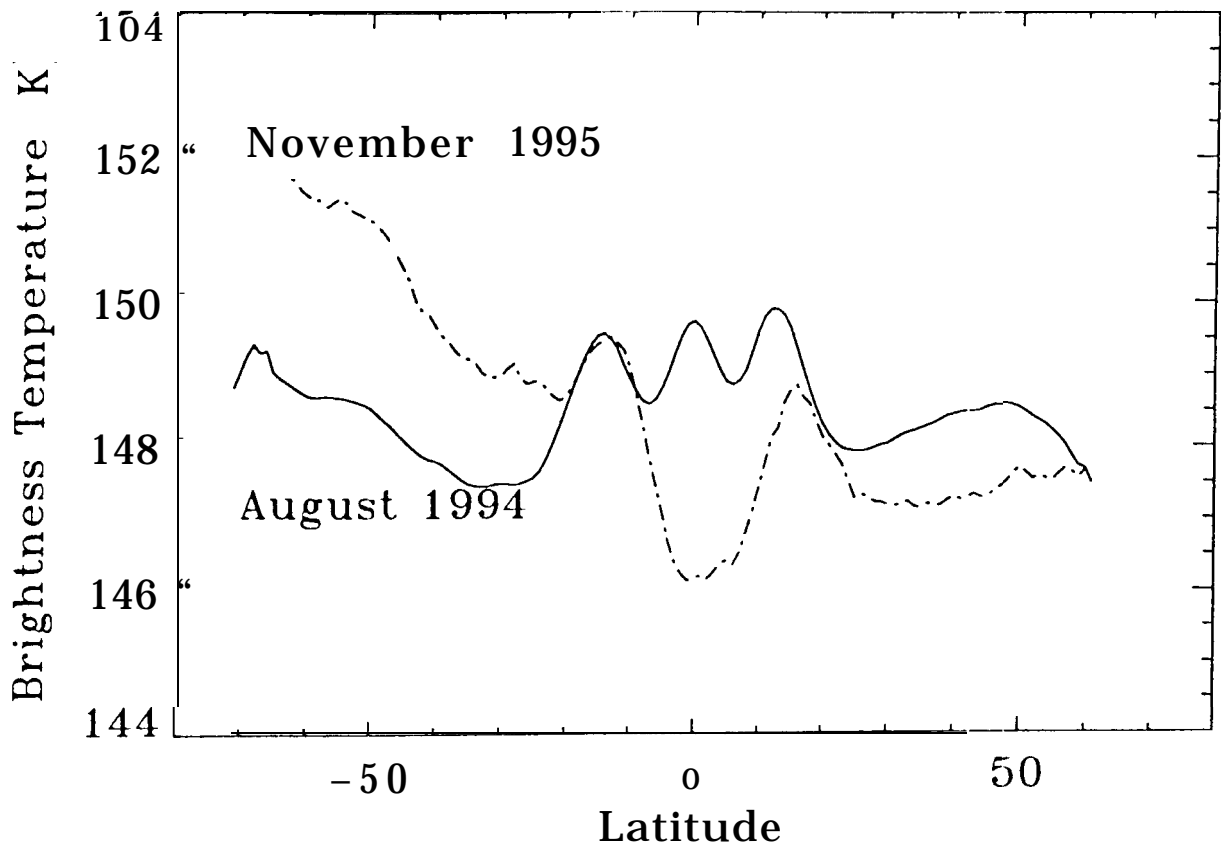


Fig 19